Protracted hydrothermal alteration recorded at the microscale in the Chenaillet ophicarbonates (Western Alps): Insights from *in situ* $\delta^{18}O$ thermometry in serpentine, carbonate and magnetite

Maria Rosa Scicchitano[a, b, *], Romain Lafay[c], John W. Valley[b], Noriko T. Kita[b], William O. Nachlas[b]

[a] Deutsches GeoForschungsZentrum GFZ, D14473 Potsdam, Germany (maria.rosa.scicchitano@gfz-potsdam.de)

[b] Department of Geoscience, University of Wisconsin, Madison 53706, WI, USA (valley@geology.wisc.edu, noriko@geology.wisc.edu, nachlas@wisc.edu)

[c] Géosciences Montpellier, Université Montpellier-II, 34095 Montpellier, France (romain.lafay@yahoo.fr)

* Corresponding author. E-mail: maria.rosa.scicchitano@gfz-potsdam.de

Keywords: ophicarbonates, Alps, oxygen isotopes, geothermometry, SIMS

Abstract

The study of serpentinites and ophicarbonates from ophiolitic terrains provides a three-dimensional perspective on the hydration and carbonation processes affecting modern oceanic lithosphere. The Chenaillet ophiolite (western Alps) is interpreted as a fragment of an oceanic core complex that resembles a modern slow spreading center, and it was weakly affected by Alpine metamorphism. Ophicarbonates from the Chenaillet ophiolite were targeted in this study for *in situ* analysis by Secondary Ion Mass Spectrometry (SIMS) of oxygen and carbon isotopes in serpentine, calcite, dolomite and magnetite. The high spatial resolution of SIMS allowed us to target different serpentine, carbonate and magnetite generations intergrown at scales ≤ 50 μm, and reveal systematic zoning in $\delta^{18}O$ with a range of 5.8‰ in serpentine (from 3.0 to 8.8‰, V-SMOW), 21.2‰ in carbonate (9.4 to 30.6‰), and 5.6‰ in magnetite (–5.0 to –10.6‰). Coupled analysis of oxygen isotopes in seven different touching-pairs of co-crystallized serpentine+carbonate and serpentine+magnetite provides independent constraints on both the temperatures and $\delta^{18}O_{(water)}$ values during serpentinization and carbonation responsible for the formation of the Chenaillet ophicarbonates. The new stable isotope data and thermometric estimates can be directly linked to textural and petrographic observations. These new results identify at least four different stages of hydrothermal alteration in the Chenaillet ophicarbonates: (1) peridotite hydration during seafloor exhumation at temperatures down to 200-130 °C and water $\delta^{18}O$ values varying from 5 to 2‰, as documented by serpentine+magnetite in mesh textures; (2) carbonation during exhumation near the seafloor at temperatures as low as 10 °C assuming water $\delta^{18}O$ values of –1‰, as documented by the highest oxygen isotope ratios in texturally older calcite; (3)

serpentinization and carbonation at temperatures up to 240 °C and water $\delta^{18}O$ values of 2-3‰, as documented by serpentine+magnetite in veins crosscutting mesh textures (T = 192±66 °C, $\delta^{18}O_{(water)}$ = 2±1‰, 2 standard deviation), serpentine+magnetite (T = 182±32 °C, $\delta^{18}O_{(water)}$ = 2±1‰) and serpentine+dolomite (T = 243±79 °C, $\delta^{18}O_{(water)}$ = 3±2‰) in recrystallized hourglass domains within serpentinite clasts, serpentine+dolomite (T = 229±50 °C, $\delta^{18}O_{(water)}$ = 3±1‰) and serpentine+calcite (T = 208±40 °C, $\delta^{18}O_{(water)}$ = 2±1‰) within the fine-grained calcite matrix surrounding serpentinite clasts; (4) late stage carbonation at temperatures down to 70-40 °C assuming water $\delta^{18}O$ values of 3 to –1‰, as documented by the highest oxygen isotope ratios in a large calcite vein crosscutting both serpentinite clasts and fine-grained carbonate matrix. We suggest that the textural and isotopic observations are consistent with a protracted serpentinization and carbonation of the lithospheric mantle that started during progressive exhumation to the seafloor and continued due to interaction with hot and isotopically shifted seawater, which circulated at depth in the oceanic crust and was then discharged near the seafloor, similar to modern mid-ocean ridge venting systems.

1. INTRODUCTION

Serpentinization and carbonation of ultramafic rocks occur over a wide range of environments and physical-chemical conditions. The majority of modern serpentinites form at slow and ultraslow spreading ridges during mantle unroofing and exhumation at the seafloor at temperatures varying from 500 °C to <100 °C (e.g., Mével, 2003; Barnes et al., 2009; Boudier et al., 2010; Bach et al., 2011; Rouméjon et al., 2018). Carbonation reactions resulting in the formation of veins and ophicarbonates (i.e., carbonated ultramafic breccias resulting from repeated tectonic and/or hydraulic fracturing of serpentinites) are usually associated with late stages of low-temperature alteration near the seafloor (Bonatti et al., 1974; Mével, 2003; Früh-Green et al., 2004; Manatschal and Müntener, 2009). Serpentinization of the subcontinental mantle is also documented at ocean-continent transition (OCT) boundaries (e.g., Iberia-Newfoundland rifted margins) where seawater infiltration is favored by crustal thinning and tectonic activity (e.g., Boillot et al., 1989; Skelton and Valley, 2000; Manatschal and Müntener, 2009; Schwarzenbach et al., 2013; Alt et al., 2018; Picazo et al., 2019). In addition to passive margins, serpentinization and carbonation of peridotite also occur at active margins and on continental settings. Ultramafic rocks exposed in ophiolitic terrains can undergo further hydration and carbonation due to low-temperature (<50 °C) interaction with meteoric water (e.g., Barnes and O'Neil, 1969; Barnes et al., 1978; Neal and Stanger, 1985; Streit et al., 2012; Barnes et al., 2013; Falk et al., 2016).

The study of ophiolitic terrains is fundamental to unravel the magmatic, tectonic and hydrothermal evolution of ocean basins from rift-drift and seafloor spreading stages to subduction initiation and final closure (Dilek and Furnes, 2014). In fact,

ophiolites represent an analogue for present-day oceanic crust and preserve the only evidence for ocean basins older than ~170 Ma (Dilek and Furnes, 2014; Pearce, 2014). Ophiolites provide better access than the one-dimensional drill cores from modern oceanic crust, but they often record intense alteration during their passage from rift to subduction/collision zone to mountain belt (Pierce, 2014; Staudigel et al., 2014). Constraining *P-T* conditions and fluid sources of hydration and carbonation reactions in ultramafic rocks from ophiolitic terrains is also important for better characterizing the conditions that favor dissolution and precipitation of carbonate minerals in these lithologies, with implications for better estimating the potential for permanent storage of CO_2 in ultramafic rocks (Kelemen and Matter, 2008; Kelemen et al., 2011). It is also crucial for tracing the mobilization and fluxes of water, carbon and fluid-mobile elements among Earth's different reservoirs (e.g., Scambelluri et al., 2004; Alt et al., 2012; Collins et al., 2015) and the production of fluids enriched in hydrogen, methane and other hydrocarbons both at near-surface conditions (Kelley et al., 2005; Miller et al., 2016) and in subduction zones (Vitale Brovarone et al., 2017).

Oxygen isotopes have been extensively used as geothermometers and tracers to determine the temperatures and fluid sources during peridotite hydration and carbonation in various tectonic settings (e.g., Wenner and Taylor, 1971, 1973; Agrinier and Cannat, 1997; Früh-Green et al., 1990, 1996; Barnes et al., 2009; Lafay et al., 2017; Noël et al., 2018; Rouméjon et al., 2018; Scicchitano et al., 2018a,b, 2020). This method requires knowledge of mineral-fluid or mineral-mineral oxygen isotope fractionation factors and assumption that isotope equilibrium between co-precipitated minerals and fluids was achieved and preserved. Measured $\delta^{18}O$ values in co-precipitated minerals can, then, be combined with corresponding calibrations of oxygen isotope fractionations to independently calculate both the equilibrium

127 temperature and the oxygen isotope composition of the interacting fluid. Several
128 studies (e.g., Wenner and Taylor, 1971; O'Hanley and Offler, 1992; Früh-Green et al.,
129 1996; Alt and Shanks, 2006; Barnes et al., 2009) have estimated serpentinization
130 temperatures and fluid $\delta^{18}O$ values using the equilibrium oxygen isotope fractionation
131 between coexisting serpentine and magnetite previously separated from the rock.
132 Geothermometry in carbonated serpentinites has recently been achieved using
133 carbonate clumped isotope techniques that allow calculating equilibrium temperatures
134 independently of the isotopic composition of the fluids from which carbonate formed
135 (e.g., Streit et al., 2012; Falk and Kelemen, 2015; de Obeso and Kelemen, 2018).
136 Studies based on mineral separates and clumped isotope techniques represent a
137 fundamental achievement in our understanding of the temperatures at which
138 serpentinization and carbonation of ultramafic rocks occur. Nevertheless, they likely
139 represent average estimates and overlook the larger complexity of these reactions
140 recorded at the microscale by the occurrence of multiple serpentine and carbonate
141 generations. In fact, recent *in situ* oxygen isotope studies by Secondary Ion Mass
142 Spectrometry (SIMS) in serpentinites and carbonated serpentinites from different
143 tectonic settings have shown a significant variation in the oxygen isotope composition
144 of serpentine and carbonate minerals recorded at the microscale (Noël et al., 2018;
145 Rouméjon et al., 2018; Scicchitano et al., 2018a, 2020). The high spatial resolution of
146 SIMS techniques allows the analysis of oxygen isotopes to be measured along
147 detailed traverses through co-precipitated host rock and vein minerals that are in
148 textural equilibrium at scales ≤ 50 μm (Turnier et al., 2020). Consequently, it is a
149 powerful tool for obtaining independent estimates of serpentinization temperatures
150 and fluid $\delta^{18}O$ values framed in a petrological context in rocks that record multiple
151 stages of fluid-rock interactions (e.g., Scicchitano et al., 2018b, 2020) as well as for

testing the achievement of isotopic equilibrium during serpentinization processes (e.g., Lafay et al., 2019).

In this study we apply SIMS techniques in combination with new reference materials (Scicchitano et al., 2020) to analyze oxygen and carbon isotopes in serpentine, carbonate (calcite, dolomite) and magnetite in order to unravel the complex fluid-rock history recorded at the microscale in ophicarbonate samples from the Chenaillet ophiolite. The fine-grained textures observed in the investigated samples can only be targeted by SIMS, which requires the use of matrix-matched reference materials (Valley and Kita, 2009). The new analytical capabilities provide unique constraints on oceanic hydrothermal alteration recorded in the Chenaillet ophiolite that were not resolved by earlier studies based on conventional data. Furthermore, the ability to target mineral phases that are in textural equilibrium (e.g., serpentine-carbonate, serpentine-magnetite) allowed us to constrain independently both alteration temperatures and fluid sources.

2. GEOLOGICAL SETTING AND PREVIOUS STUDIES

The Chenaillet ophiolite in the Franco-Italian Alps (Fig. 1) is interpreted as a remnant of embryonic oceanic crust formed at the distal part of a Magma-Poor-Ocean Continent Transition (MP-OCT) margin (Manatschal and Müntener, 2009; Manatschal et al., 2011; Li et al., 2013; Lafay et al., 2017) resembling actual slow spreading centers (Lagabrielle and Cannat, 1990; Lagabrielle and Lemoine, 1997). It consists mainly of pillow lavas with Mid Ocean Ridge Basalt (MORB) geochemical signature superimposed on tectonically exhumed gabbros and serpentinized mantle rocks comparable to oceanic core complexes (OCC) exposed in modern slow- to

177 ultraslow-spreading ridges (Manatschal and Müntener, 2009; Manatschal et al., 2011;
178 Li et al., 2013; Lafay et al., 2017). Recent U–Pb zircon ages in the gabbros suggest
179 that the Piemont-Liguria oceanic domain formed between 158-166 Ma (Li et al.,
180 2013). No sheeted dike complex and post-rift sedimentary cover are observed in the
181 Chenaillet ophiolite; sediments occur locally and consist of reworked mafic and
182 ultramafic rocks covered by pelagic deposits, radiolarite and limestones (Lemoine et
183 al., 1983; Manatschal et al., 2011). In contrast to other ophiolitic terrains in the Alps,
184 the Chenaillet ophiolite escaped high-pressure metamorphism during the Late
185 Cretaceous to Eocene Alpine subduction and was only weakly overprinted by
186 subgreenschist to lower greenschist facies metamorphism during thrusting onto the
187 European margin (Mével et al., 1978; Goffé et al., 2004; Manatschal and Müntener,
188 2009; Manatschal et al., 2011). High- to low-temperature hydrothermal processes in
189 the Chenaillet ophiolite occurred in an oceanic setting prior to obduction and are
190 represented by mylonitized amphibole-bearing gabbros (Mével et al., 1978),
191 serpentinites and ophicarbonates (Manatschal and Müntener, 2009; Lafay et al.,
192 2017). Serpentinization of mantle rocks is pervasive and original silicate minerals
193 from the igneous stage are usually replaced by mesh and bastite textures typical of
194 seafloor alteration under static conditions (Andreani et al., 2007; Manatschal and
195 Müntener, 2009; Manatschal et al., 2011; Lafay et al., 2017). The pioneering work of
196 Lemoine et al. (1983) and Lagabrielle and Lemoine (1997) has been recently
197 reconsidered by Lafay et al. (2017) who provided a detailed petrological, geochemical
198 and stable isotope (O, C, H) study of ophicarbonates from the Chenaillet ophiolite.
199 These rocks consist of few tens of meter thick layers (Fig. 1b) of breccia found atop
200 massive serpentinites near the serpentinite-basalt transition. Ophicarbonate breccias
201 are made of slightly rounded serpentinite clasts cemented by a matrix of small (~12

μm in average) calcite grains (Lemoine et al., 1983; Lafay et al., 2017) (Fig. A.1). The diversity of microstructures (veins, replacement, matrix) allowed the authors to identify multiple events of carbonation following initial serpentinization of peridotites, which were attributed to a progressive cooling during exhumation of the mantle at the seafloor (Lafay et al., 2017). However, values of $\delta^{18}O$ in serpentine (3.3 to 5.1‰) and carbonates (11 to 16‰) could suggest that both serpentinization and carbonation occurred at higher temperatures (T = 155-190 °C and 110-180 °C, respectively) than seafloor alteration (Lafay et al., 2017). These temperature estimates should be reexamined. They were calculated assuming a constant unaltered seawater composition (Lafay et al., 2017) and homogenous mineral grains. However, the microstructures and chemical zoning suggest that the micro-drilling technique used to select serpentine and carbonate for stable isotope analyses has mixed different generations resulting in average compositions. In light of recent analytical developments allowing accurate *in situ* analysis of oxygen and carbon isotopes in serpentine, magnetite and carbonate by SIMS (Valley and Kita, 2009; Huberty et al.., 2010; Kita et al., 2011; Śliwiński et al., 2015a,b; Scicchitano et al., 2018a, 2020), a number of ophicarbonates studied by Lafay et al. (2017) were reanalyzed for stable isotope ratios (O, C) by SIMS to: (i) target the various serpentine and carbonate generations identified by Lafay et al. (2017) that could not be separated with micro-drilling techniques due to their fine-grained size, (ii) identify systematic isotopic zoning recorded at the microscale in both serpentine and carbonate, (iii) couple *in situ* analysis of oxygen isotopes in potentially co-crystallized minerals (serpentine-calcite, serpentine-dolomite, calcite-dolomite, serpentine-magnetite) to estimate the equilibrium temperature independently of the fluid composition. To the best of our knowledge, this study represents the first successful attempt to applying the

serpentine-magnetite geothermometer at the microscale and provides the first stable isotope data in dolomite in these samples that could not be targeted by previous studies due to its small grain size.

3. PREPARATION OF GRAIN MOUNTS AND ANALYTICAL METHODS

Five ophicarbonate samples (RL3, RL6, RL7, RL9 and RL10) from the Chenaillet ophiolite previously characterized by Lafay et al. (2017) were prepared for oxygen and carbon isotope analysis by SIMS, as described in the Electronic Appendix A.

A Hitachi S3400 Variable Pressure (VP) Scanning Electron Microscope (SEM) at the Department of Geoscience (University of Wisconsin-Madison, UW-Madison) was operated at low (P = 30 Pa) and high vacuum in backscattered electron (BSE) mode to identify the different generations of serpentine, carbonate and magnetite in the Chenaillet ophicarbonates described by Lafay et al. (2017). Carbonate minerals were also imaged using a cathodoluminescence (CL) Gatan PanaCL/F system. Careful SEM imaging in BSE, secondary electron (SE) and CL modes was performed following each SIMS session to check the location and features of all SIMS pits. We rejected analyses where pits were located on fractures, mixed domains or other features that could alter isotope ratios. Prior to SEM analysis, mounts were coated with carbon or a thin layer of gold; to avoid affecting carbon isotope ratios during SIMS analysis in carbonates, no carbon coating was used on the corresponding mounts. The accelerating voltage and working distance were usually ~15 or 10 kV and ~10 or 15 mm for BSE and CL imaging, respectively.

Serpentine, calcite, dolomite and magnetite from the Chenaillet ophicarbonates were analyzed for major and minor element mineral chemistry using a CAMECA

252 SXFive Field Emission Electron Microprobe (EPMA) at the Department of
253 Geoscience (UW-Madison). Details of EPMA methods are given in the Electronic
254 Appendix A. Direct analysis of oxygen with EPMA was necessary for accurate
255 quantification of variable Fe oxidation in serpentine and magnetite and variable water
256 contents in serpentine. All serpentine analyses were normalized to 18 (O + OH)
257 according to the general formula $Mg_6Si_4O_{10}(OH)_8$. Approximate H_2O content (wt.%)
258 was calculated based on excess oxygen values measured by EPMA assuming total
259 iron as Fe^{2+} (Table A.1). Carbonate analyses were normalized to 6 O according to the
260 general formula $(Ca,Mg)_2(CO_3)_2$ (Table A.2). Magnetite analyses were normalized to
261 3 cations according to the general formula Fe_3O_4, and approximate Fe^{3+} and Fe^{2+}
262 contents were estimated by charge balance (Table A.3).
263 A CAMECA IMS-1280 large radius multicollector secondary ion mass
264 spectrometer at the WiscSIMS laboratory (UW-Madison) was used to perform *in situ*
265 oxygen and carbon isotope analyses of serpentine, carbonate and magnetite in the
266 Chenaillet ophicarbonates during seven analytical sessions (Tables A.1 to A.4).
267 Details on analytical settings are given in the Electronic Appendix A. We monitored
268 bias, drift and external precision during each analytical session by bracketing 10-20
269 unknown analyses with at least eight analyses of the reference material located in the
270 same grain mount. Matrix effects on bias due to variations in Mg/Fe ratios in
271 serpentine and dolomite-ankerite solid solutions, which are observed during oxygen
272 and carbon isotope analysis by SIMS (Śliwiński et al., 2015a,b; Scicchitano et al.,
273 2020), were monitored and quantified for each analytical session by constructing a
274 calibration curve using a suite of serpentine and carbonate reference materials (Table
275 A.4). These calibration curves were then used to correct $\delta^{18}O$ and $\delta^{13}C$ values
276 measured in serpentine and dolomite from the Chenaillet ophicarbonates. Orientation

effects in chrysotile were estimated by analyzing two different orientations of the chrysotile C22908 reference material as described in Scicchitano et al. (2018a, 2020), while orientation effects in magnetite were minimized using a special 3 kV protocol (see Electronic Appendix A for details) and evaluated by analyzing ~30 grains with different orientation of the magnetite M7-5830 reference material (Huberty et al., 2010; Kita et al., 2011).

4. RESULTS

4.1. Petrography and mineral chemistry

For the purpose of this study, we summarize the main textures targeted for *in situ* analysis by SIMS, which are essential for putting into petrological context the new oxygen and carbon isotope data.

4.1.1. Serpentine

Serpentine is the main constituent of the serpentinite clasts where it forms either mesh textures characterized by well-defined cores and rims (Fig. 2a-c) or hourglass textures in which a distinction between mesh rim and mesh center is not possible (Fig. 2d). Raman spectroscopy showed that mesh cores consist of a mixture between lizardite and chrysotile (hereafter referred to as "serpentine"), whereas mesh rims consist of pure lizardite (Lafay et al., 2017). Magnetite (up to ~20 μm large) is often observed around mesh cores in sample RL6 (Fig. 2b), while it is usually lacking or very limited in mesh textures of other samples. It is occasionally possible to identify an inner and outer mesh

core both surrounded by magnetite (Fig. 2b). A complex network of mesh veinlets (V-1) consisting of lizardite+magnetite follows original (pristine silicate) grain boundaries (Fig. 2e-f), while larger lizardite+magnetite veins 250 μm in width (V-2) crosscut mesh and hourglass textures (Fig. 2g). In sample RL6, lizardite+dolomite layers are observed within the carbonate matrix (Fig. 2j-k); this serpentine generation is hereafter referred to as "matrix serpentine". Finally, small chrysotile aggregates up to a few tens of μm large (Lafay et al., 2017) are widespread in the carbonate matrix surrounding serpentinite clasts (Fig. 2k-l).

Mesh cores have higher Mg numbers [Mg# = 100 × Mg/(Mg+Fe), molar, with Fe = Fe(total)] and silica contents relative to mesh rims in all samples (Fig. A.2). In particular, mesh cores in samples RL6, RL7 and RL9 have Mg# ranging between 96 and 99 mole % and SiO_2 contents ranging between 40.6 and 43.4 wt.%, whereas mesh rims have Mg# of 90 to 97 mole % and SiO_2 contents of 38.0 to 42.0 wt.% (Fig. A.2, Table A.1). A similar trend between Mg# and silica is observed in mesh textures from samples RL10 and RL3, which however show lower Mg# (91 to 95 mole % in mesh cores, 85 to 95 mole % in mesh rims) and comparable SiO_2 contents (39.9 to 42.5 wt.% in mesh cores, 36.0 to 42.8 wt.% in mesh rims) relative to mesh serpentine in the other three samples (Fig. A.2, Table A.1). The variability in alumina content is lower in mesh serpentine from samples RL6, RL7 and RL9 (Al_2O_3 = 0.2-1.3 wt.%) relative to mesh serpentine from samples RL10 and RL3 (Al_2O_3 = 0.1-4.3 wt.%) (Fig. A.2, Table A.1). Serpentine in hourglass textures has a similar chemical composition as serpentine in mesh rims (Fig. A.2, Table A.1). Lizardite in V-1 veins has similar silica (SiO_2 = 41.2-43.1 wt.%) and alumina contents (Al_2O_3 = 0.1-0.6 wt.%) across different samples, whereas Mg# decreases from sample RL9 (Mg# = 96-97) to samples RL10 and RL3 (Mg# = 94-95) (Fig. A.2, Table A.1). Lizardite in V-2 veins and "matrix serpentine"

observed in sample RL6 have similar chemical compositions as those of mesh cores in the same sample (Fig. A.2, Table A.1). Chrysotile in the carbonate matrix surrounding serpentinite clasts is also characterized by higher Mg# in samples RL6, RL7 and RL9 (Mg# = 94-98) relative to samples RL10 and RL3 (Mg# = 88-95; Fig. A.2, Table A.1); in contrast, both silica and alumina contents are similar across different samples (SiO_2 = 39.5-44.2 wt.%, Al_2O_3 = 0.2-2.2 wt.%).

4.1.2. Carbonates within serpentinite clasts

Serpentine in mesh cores is often partially or completely replaced by calcite (hereafter referred to as C2, Lafay et al., 2017) and relict serpentine inclusions are frequently observed in calcite mesh (Fig. 2a-c). C2 calcite is sometimes connected to calcite veinlets ~10 μm in width (hereafter C1; Lafay et al., 2017); the largest C1 calcite veins (up to 500 μm in width) crosscut serpentine in mesh and hourglass textures as well as V-1 and V-2 lizardite+magnetite veins (Fig. 2h-i). Although C1 calcite veins are usually restricted to individual clasts and are often truncated at the edges of the clasts, they sometimes propagate into the surrounding carbonate matrix (Fig. A.1). SEM-CL imaging shows complex patchy zoning and resorption features in both C1 veins and C2 mesh suggesting multiple events of recrystallization (Fig. 3). As previously shown by Lafay et al. (2017), the edges of C1 calcite veins are sometimes delimited by distinct CL calcite rims (Fig. 3b-c).

In addition to calcite, subordinate dolomite is observed in some samples as (i) rims around C2 calcite mesh (Fig. 3e, 4a), (ii) borders along C1 veins at the boundary with serpentine (Fig. 3a, 4b), (iii) subhedral grains associated with “matrix serpentine” in sample RL6 (Fig. 2k, 4c) and (iv) veinlets in the C3 calcite matrix.

No significant variation is observed in the chemical composition of calcite in different textures across different samples (Table A.2). FeO and MnO contents are usually <0.5 wt.% with the exception of calcite in C2 mesh (FeO = 0.1-1.3 wt.%) from sample RL6. In contrast, the MgO content in calcite from different textures has a larger variability from 0.02 to 1.6 wt.% (Table A.2).

Dolomite has a similar chemical composition in all samples and textural locations with FeO content varying from 0.1 to 1.2 wt.% and MnO content <0.3 wt.%; Fe# is <3 mole %.

4.1.3. Carbonates surrounding serpentinite clasts

Serpentinite clasts are embedded in a calcite matrix (hereafter C3; Lafay et al., 2017) that appears either "turbid", when intergrown with fine-grained chrysotile aggregates as documented through Raman spectroscopy (Lafay et al., 2017), or "clear", when no chrysotile is present (Fig. A.3). Clear calcite domains (hereafter C1') in the C3 calcite matrix were interpreted by Lafay et al. (2017) as remnants of C1 veins channeling fluids. Calcite veins ~100 μm in width (hereafter C3-veins) sometimes crosscut the C3 calcite matrix but not the lizardite+dolomite layers (Fig. 2j). Finally, a large calcite vein ~5 mm in width (hereafter C4; Lafay et al., 2017) crosscuts both C3 calcite matrix and serpentinite clasts in sample RL9 (Fig. A.1). SEM-CL imaging shows that C1' clear calcite domains consist of large calcite grains that sometimes exhibit a concentric (Fig. 5a-b) or oscillatory CL zoning (Fig. 5c) truncated by the surrounding aggregates of fine-grained C3 calcite matrix; the latter also shows a similar concentric CL zoning (Fig. 5a, d). Calcite grains in C1' are often crosscut or bounded by later calcite veinlets (hereafter C1'-veins) (Fig. 5a, c). In contrast, C3-veins do not exhibit complex CL

zoning (Fig. 5d). In addition to calcite, dolomite was observed at the boundary between C4 vein and serpentinite clast in sample RL9 (Fig. 4d).

FeO and MnO contents are usually <0.5 wt.% with the exception of calcite in C3-veins (MnO = 0.1-0.7 wt.%) from sample RL6. In contrast, the MgO content in calcite from different textures has a larger variability from 0.03 to 1.9 wt.% (Table A.2). No significant variation is observed between different textures across different samples.

4.2. Oxygen and carbon isotopes by SIMS

4.2.1. Serpentine

In situ oxygen isotope analyses of serpentine were performed in two analytical sessions (S1 and S2; Table A.1). A suite of six (S1) to seven (S2) antigorite reference materials was analyzed at the beginning of each analytical session in order to build a calibration curve for the correction of polymorph-specific matrix effects due to Mg/Fe variations in the compositional range Mg# = 77.5-99.5 (Table S2 in Scicchitano et al., 2020). Lizardite (L3431) and chrysotile (C22908) reference materials (Scicchitano et al., 2018a, 2020) were also analyzed to correct for the bias relative to the normalizing antigorite reference material Al06-44A (Table S2 in Scicchitano et al., 2020). A bias of ~1‰ was measured between lizardite L3431 and antigorite Al06-44A in both analytical sessions. Orientation effects in chrysotile C22908 were ~1‰ in all analytical sessions, hence this is considered as a limitation on the accuracy of analyses done in this polymorph, but no orientation effects are detected for lizardite or antigorite. Measured $\delta^{18}O$ values in serpentine from the Chenaillet ophicarbonates

were corrected according to the method described in Scicchitano et al. (2020) and are reported relative to the V-SMOW scale (Table A.1).

The highest average $\delta^{18}O$ values are recorded in the core of mesh textures where oxygen isotope ratios vary between 4.4 and 8.5‰ with no distinction between calcite-free and calcite-bearing mesh cores (Fig. 6). Although mesh rims show a large variability in oxygen isotope ratios with $\delta^{18}O$ values varying from 4.5 to 8.8‰, their average $\delta^{18}O$ values are generally lower compared to mesh cores (Fig. 6). No correlation between $\delta^{18}O$ value and Mg# was observed in mesh textures. Lizardite in V-1 veins has an oxygen isotope composition varying from 3.5 to 6.4‰ with average $\delta^{18}O$ values lower relative to mesh rims (Fig. 6). Lizardite in V-2 veins crosscutting both V-1 veins and mesh textures has low $\delta^{18}O$ values of 3.2-4.2‰ (Fig. 6). Similar low oxygen isotope ratios relative to mesh cores are recorded in hourglass serpentine ($\delta^{18}O$ = 3.8-5.7‰), "matrix serpentine" ($\delta^{18}O$ = 3.1-5.4‰) and serpentine in the C4 calcite vein ($\delta^{18}O$ = 4.0-4.8‰) (Fig. 6). Chrysotile in the C3 calcite matrix has a large variability in $\delta^{18}O$ values from 3.0 to 5.7‰ (Fig. 6).

Overall, SIMS analyses allow identifying a larger variation in serpentine $\delta^{18}O$ values (from 3.0 to 8.8‰) relative to previous studies on powdered micro-drilled samples ($\delta^{18}O$ = 3.3-5.1‰; Lafay et al., 2017) as well as a systematic variation in $\delta^{18}O$ values between different serpentine generations.

4.2.2. Carbonate

In situ oxygen and carbon isotope analyses in carbonates were performed in four analytical sessions (S3 to S5 for O, S6 for C; Table A.2). Calcite UWC-3 (Kozdon et al., 2009) was used as a working reference material. A suite of seven to ten carbonate

426 reference materials was analyzed at the start of each session to calibrate matrix effects
427 in samples with chemical composition along the dolomite-ankerite solid solution
428 series (Table A.4). Measured $\delta^{18}O$ and $\delta^{13}C$ values in dolomite from the Chenaillet
429 ophicarbonates were corrected according to the method described in Śliwiński et al.
430 (2015a,b) and for the bias between dolomite UW6220 and calcite UWC-3 reference
431 materials (Table A.2). Values of $\delta^{18}O$ and $\delta^{13}C$ are reported relative to the V-SMOW
432 and V-PDB scales, respectively (Table A.2).

433 Values of $\delta^{18}O$ for calcite in C1 veins mostly range between 9.4 and 13.9‰ and
434 occasionally up to 22.3‰ (Fig. 7). The highest $\delta^{18}O$ values are commonly observed at
435 the edges of large C1 veins (Fig. 3b). Analyses performed across one of the largest C1
436 veins (Fig. 3c, A.4a) showed a nearly symmetric edge-to-edge oxygen isotope zoning
437 up to ~3‰ with the lowest $\delta^{18}O$ values in the core of the vein (Fig. A.4). Values of
438 $\delta^{13}C$ for C1 calcite veins vary between –0.6 and 2.4‰ but no systematic correlation is
439 observed with textures (Fig. A.5). Calcite in C2 mesh textures shows the largest
440 variability in oxygen isotope composition with $\delta^{18}O$ values ranging from 9.8 to
441 30.6‰ (Fig. 7), whereas $\delta^{13}C$ values vary between –2.6 and 1.9‰ (Fig. A.5). The
442 highest $\delta^{18}O$ values in C2 calcite mesh are typically observed at the core of mesh
443 textures, whereas the edges usually have lower $\delta^{18}O$ values (Fig. 3d-i). It is sometimes
444 possible to observe resorption textures where calcite with low $\delta^{18}O$ values, similar to
445 those measured in nearby C1 veinlets, replaces C2 calcite mesh cores with higher
446 $\delta^{18}O$ values (Fig. 3f-i). Calcite in C1' textures also shows a large variability in oxygen
447 and carbon isotopes similar to C2 calcite mesh with $\delta^{18}O$ and $\delta^{13}C$ values of 10.6 to
448 24.9‰ and –1.1 to 1.6‰, respectively (Fig. 7, A.5). Similar to calcite in C2 mesh
449 textures, the highest $\delta^{18}O$ values in C1' textures are commonly observed in the cores
450 of large calcite grains (Fig. 5 and Electronic Appendix B). Late C1'-veins

crosscutting or bounding C1' calcite grains have low $\delta^{18}O$ values of 10.9 to 11.8‰ (Fig. 5c, 7 and Electronic Appendix B) and $\delta^{13}C$ values of –0.6 to 0.7‰ (Fig. A.5). Similarly, calcite in the fine-grained C3 matrix and crosscutting C3-veins also have low $\delta^{18}O$ values of 9.8-12.9‰ and 10.5-11.5‰, respectively (Fig. 5d, 7 and B.1 in Electronic Appendix B); $\delta^{13}C$ values vary from –0.1 to 2.2‰ and –0.6 to 0.6‰, respectively (Fig. A.5). Finally, calcite in the latest C4 vein has the highest average oxygen isotope composition (average $\delta^{18}O$ = 21.1‰, Fig. 7) and carbon isotope values similar to calcite in other textural locations ($\delta^{13}C$ = –0.7 to 1.7‰, Fig. A.5). Dolomite associated with mesh textures in serpentinite clasts has $\delta^{18}O$ values of 10.7 to 14.1‰ (n = 20) that are comparable to the oxygen isotope composition of dolomite bordering C1 calcite veins ($\delta^{18}O$ = 10.1-11.9‰, n = 9) and the C4 vein ($\delta^{18}O$ = 11.2-12.5‰, n = 2) (Table A.2). Similar $\delta^{18}O$ values are also recorded in subhedral dolomite associated with matrix serpentine in the layers at the boundary between serpentinite clasts and C3 calcite matrix ($\delta^{18}O$ = 11.4-13.2‰, n = 5) (Table A.2).

SIMS analyses show a much larger variability (~21‰) in calcite $\delta^{18}O$ values relative to ~6‰ variation described in Lafay et al. (2017). Additionally, the ability to place SIMS data into a petrological context highlights that higher $\delta^{18}O$ values in zoned C1 veins, C2 mesh and C1' calcite domains likely represent an older signature that is progressively replaced by younger calcite generations with lower $\delta^{18}O$ values (core of C1 veins, C1'-veins, C3 matrix and C3-veins). SEM-CL imaging linked to oxygen isotope ratios also allowed distinguishing C1' domains from C1 open veins. Values of $\delta^{18}O$ increase again in the latest C4 calcite vein (average $\delta^{18}O$ = 21.1‰) crosscutting serpentinite clasts and C3 calcite matrix (average $\delta^{18}O$ = 11.1‰). Values of $\delta^{13}C$ measured by SIMS vary by ~4.5‰ at most in C2 calcite mesh, similar to the variation observed by Lafay et al. (2017). Nevertheless, SIMS analyses are generally

476 higher relative to those reported in Lafay et al. (2017) (–2.6 to +2.4‰ vs. –5.2 to
477 +0.4‰, respectively).
478
479 **4.2.3. Magnetite**
480
481 *In situ* oxygen isotope analyses in magnetite were performed in one analytical
482 session (S7; Table A.3). The extent of crystal orientation effects in magnetite was
483 determined by bracketing analyses of the M7-5830 magnetite reference material with
484 eight analyses of the UWQ-1 quartz reference material (Kelly et al., 2007) (Table
485 A.4). A grain-to-grain reproducibility of ~1‰ (2 standard deviations, 2SD) was
486 obtained (using the low-kV protocol of Kita et al., 2011) in both M7-5830 and UWQ-
487 1 (Table A.4); hence this represents the maximum precision achievable during oxygen
488 isotope analyses of magnetite in this study. Magnetite analyses in the ophicarbonate
489 samples from the Chenaillet ophiolite were bracketed with eight analyses in the
490 UWC-3 calcite reference material (Kozdon et al., 2009) located in the same grain
491 mounts in order to monitor bias, drift and external precision (Table A.3). Magnetite
492 analyses were corrected for the bias between UWC-3 calcite and M7-5830 magnetite
493 reference materials measured in different mounts, and they are reported relative to the
494 V-SMOW scale (Tables A.3 and A.4).
495 Magnetite grains larger than ~10 μm located in different textures (mesh, V-1 and
496 V-2 veins, hourglass serpentine) were targeted for SIMS oxygen isotopes analysis in
497 samples RL6, RL3 and RL9 (Table A.3). Magnetite in mesh textures (Fig. 2b and
498 A.6a) shows the largest variability in $\delta^{18}O$ values from –10.6 to –5.0‰ (n = 32).
499 Magnetite in V-1 veins (Fig. 2f and A.6b) and V-2 veins (Fig. 2g and A.6c) has
500 oxygen isotope ratios varying from –8.5 to –7.3‰ (n = 3) and –7.7 to –10.6‰ (n = 2),

501 respectively. Magnetite associated with hourglass serpentine (Fig. 2d and A.6d) has
502 an oxygen isotope composition of –9.6 to –8.0‰ (n = 4).
503
504 **5. DISCUSSION**
505
506 **5.1. Estimating alteration temperatures and water $\delta^{18}O$ values in co-crystallized**
507 **mineral pairs**
508
509 Based on textural observations, we identified seven pairs of minerals that appear to
510 be in textural equilibrium along the metasomatic sequence and, therefore, assumed to
511 have co-crystallized: (i) lizardite+magnetite in mesh textures with a single mesh core,
512 V-1 veins (Fig. 2e, f), V-2 veins (Fig. 2g), and in the hourglass matrix (Fig. 2d); (ii)
513 lizardite+dolomite in the layers at the boundary between serpentinite clast and
514 carbonate matrix (Fig. 2k and 4c) as well as with hourglass serpentine (Fig. 4b, d);
515 (iii) chrysotile+calcite in the C3 calcite matrix (Fig. 2l). Coupled oxygen isotope
516 analysis by SIMS in these mineral pairs allows us to test whether isotopic equilibrium
517 was achieved during hydration and carbonation reactions, in which case equilibrium
518 temperatures and water $\delta^{18}O$ values are independently estimated.
519
520 **5.1.1. Serpentine-magnetite**
521
522 The majority of targeted serpentine-magnetite pairs (n = 17, Table 1) are in mesh
523 textures (sample RL6) because of the larger (>10 μm) size of magnetite grains. Only a
524 limited number of analyses was possible in V-1 veins (n = 1), V-2 veins (n = 2) and
525 hourglass matrix (n = 4) because of the small grain size of magnetite (Table 1).

526 A large uncertainty exists on the serpentine-water oxygen isotope fractionation
527 because different calibrations (Wenner and Taylor, 1971; Savin and Lee, 1988; Früh-
528 Green et al., 1996; Zheng, 1993; Saccocia et al., 2009) disagree by >4‰ and up to
529 ~20‰ when extrapolated to temperatures <200 °C (see Fig. 10 and discussion in
530 Scicchitano et al., 2020). In this study, the preferred calibrations for calculating the
531 equilibrium temperature for each serpentine-magnetite pair are the serpentine-water
532 oxygen isotope fractionation factors of Früh-Green et al. (1996) and the magnetite-
533 water oxygen isotope fractionation factors of Bottinga and Javoy (1973). The same
534 calibrations were then used to calculate the oxygen isotope composition of water in
535 equilibrium with both serpentine and magnetite at each equilibrium temperature
536 (Table 1 and Fig. 8). For mesh cores, equilibrium temperatures vary from 204 °C to
537 132 °C and $\delta^{18}O_{(water)}$ values decrease with temperature from 5.2 to 1.8‰ (Fig. 8). For
538 serpentine-magnetite pairs in V-1 veins, V-2 veins and hourglass textures, equilibrium
539 temperatures vary from 173 °C, 169-215 °C and 162-198 °C, respectively, while
540 water $\delta^{18}O$ values vary between ~1 and 3‰ (Fig. 8).
541 For comparison, equilibrium temperatures and $\delta^{18}O_{(water)}$ values were also
542 calculated using other calibrations. Estimates calculated by combining the serpentine-
543 water oxygen isotope fractionation factors of Saccocia et al. (2009) with the
544 magnetite-water oxygen isotope fractionation factors of Bottinga and Javoy (1973)
545 differ by ~50 °C (from 261 to 191 °C) and ~1‰ (from ~4 to 0‰), respectively,
546 relative to estimates derived from the calibration by Früh-Green et al. (1996) (Fig. 8
547 and Table 1). Temperatures calculated with the calibration of Saccocia et al. (2009)
548 could be overestimated of up to 40 °C (at exchange fraction < 40%) due to a bias in
549 their serpentine-water calibration resulting from extrapolation of equilibrium
550 fractionation factors in three-exchange site systems using the methods described by

551 Northrop and Clayton (1966) or Zheng et al. (1994), which are valid for two-
552 exchange site systems (Agrinier and Javoy, 2016). Equilibrium temperatures
553 calculated by combining the serpentine-water and magnetite-water oxygen isotope
554 fractionation factors of Zheng (1991, 1993) as well as the serpentine-magnetite
555 calibration by Früh-Green et al. (1996; their Eq. 3) are ~50-70 °C lower than those
556 estimated using the serpentine-water and magnetite-water calibrations by Früh-Green
557 et al. (1996) and Bottinga and Javoy (1973) (Table A.5). Considering the maximum
558 uncertainties derived from the various calibration equations and $\delta^{18}O$ measurements,
559 we estimate a total uncertainty of ±80 °C on the calculated equilibrium temperatures.
560 The uncertainty on $\delta^{18}O_{(water)}$ values is estimated to be in the order of ±1‰.
561
562 **5.1.2. Serpentine-dolomite**
563
564 Lizardite and subhedral dolomite grains in the layers at the boundary between
565 serpentinite clast and carbonate matrix are relatively homogenous in oxygen isotopes
566 with average $\delta^{18}O$ values of 4.7±1.4‰ (2SD, n = 10) and 12.2±1.3‰ (2SD, n = 5),
567 respectively, suggesting that they are in isotopic equilibrium. Using the average $\delta^{18}O$
568 values measured by SIMS, we calculated an oxygen isotope fractionation ($\Delta^{18}O_{Dol\text{-}Srp}$)
569 of 7.5‰, which corresponds to an equilibrium temperature of 229 °C (Fig 9a). In
570 order to calculate the temperature at which serpentine and dolomite formed, we used
571 the empirical calibration of the serpentine-water oxygen isotope fractionation by
572 Früh-Green et al. (1996) and the calibration of the dolomite-water oxygen isotope
573 fractionation (experiments at T = 252-292 °C, Matthews and Katz, 1977).
574 Extrapolation of the experimental calibration by Saccocia et al. (2009) would result
575 in an unrealistically high equilibrium temperature (even if accounting for the bias

576 described by Agrinier and Javoy, 2016) given a maximum calculated $\Delta^{18}O_{Dol\text{-}Srp}$ of
577 5.6‰ is obtained assuming T = 500 °C, which is the maximum thermal stability of
578 serpentine in oceanic settings (e.g., Mével, 2003). Consequently, we consider
579 extrapolation of the empirical calibration by Früh-Green et al. (1996) more reliable.
580 At a temperature of 229 °C, serpentine and dolomite would be in equilibrium with a
581 fluid of 3.3‰ (Fig. 9b). Similar equilibrium temperature of 240 °C and water $\delta^{18}O$
582 value of 3.3‰ are calculated using the average oxygen isotope ratios measured in
583 hourglass serpentine and dolomite pairs (Table 2, Fig. 9). These estimates are within
584 uncertainty of those calculated for lizardite+magnetite pairs in hourglass textures.
585
586 **5.1.3. Serpentine-calcite**
587
588 Calcite in the fine-grained C3 matrix and the co-crystallized fine-grained chrysotile
589 have average $\delta^{18}O$ values of 11.1±1.2‰ (2SD, n = 57) and 3.9±1.4‰ (2SD, n = 22),
590 respectively, corresponding to a $\Delta^{18}O_{Cal\text{-}Srp}$ of 7.2‰ (Fig. 9a). Combining the
591 empirical calibration of the serpentine-water system by Früh-Green et al. (1996) with
592 the experimental calibration of the calcite-water oxygen isotope fractionation
593 (experiments at T = 0-500°C, O'Neil et al., 1969), yields an equilibrium temperature
594 of 208 °C and a $\delta^{18}O_{(water)}$ of 2.0‰ (Fig. 9). The calibration by O'Neil et al. (1969) is
595 in good agreement with experimental calibrations by Golyshev et al. (1981) and Kim
596 and O'Neil (1997). As for the dolomite-serpentine pair, the experimental calibration
597 by Saccocia et al. (2009) for the calcite-serpentine pair would result in unrealistically
598 high equilibrium temperature not consistent with seafloor serpentinization (T >500
599 °C).
600

601 **5.2. Evolution model for the hydrothermal alteration in the Chenaillet ophiolite**

602

603 In the following discussion, stable isotope data are combined with petrographic
604 observations and well-documented geological context to reconstruct the main phases
605 of fluid-rock interaction recorded in the Chenaillet ophicarbonates (Fig. 10, 11).
606 Alteration temperatures and water oxygen isotope compositions estimated
607 independently from mineral-mineral pairs (see above) are used as anchor points for
608 the interpretations.

609

610 **5.2.1. Exhumation to the seafloor: early serpentinization followed by low-*T***
611 **carbonation**

612

613 Oxygen isotope values of serpentine increase from V-1 mesh veins ($\delta^{18}O$ = 3.5 to
614 6.4‰) to mesh cores ($\delta^{18}O$ = 4.4 to 8.5‰), with no distinction between carbonate-free
615 and carbonate-bearing mesh textures (Fig. 6, 10). Additionally, serpentine in mesh
616 textures associated with magnetite has similar oxygen isotope and chemical
617 compositions as serpentine in magnetite-free mesh textures from the same sample.
618 Hence, we assume that the formation of serpentine in different mesh cores (i.e.,
619 magnetite- and calcite-bearing versus magnetite- and calcite-free) is attributable to the
620 same hydrothermal event. The physical-chemical conditions at which serpentine in V-
621 1 mesh veins and mesh rims formed cannot be independently constrained, but it is
622 likely that they record the earliest stages of alteration with V-1 veins acting as
623 conduicts that allowed progressive fluid percolation and pervasive replacement in
624 mesh cores. The variation in Mg# and Al_2O_3 observed in mesh textures from samples
625 RL6, RL7 and RL9 versus samples RL10 and RL3 (Fig. A.2) suggests formation of

626 serpentine after olivine versus pyroxene, respectively (e.g., Deschamps et al., 2013).
627 Because no relict pyroxene and olivine are observed in any of the investigated
628 samples, it is possible that serpentinization started at T>400 °C (favoring rapid
629 dissolution of orthopyroxene) and then proceeded at T<300 °C (favoring rapid
630 dissolution of olivine), as documented by experimental studies (e.g., Martin and Fyfe,
631 1970; Allen and Seyfried, 2003). The limited occurrence of antigorite, chlorite and
632 tremolite in the Chenaillet ophicarbonates (Lafay et al., 2017) is consistent, in fact,
633 with greenschist facies conditions (T = 300-500 °C). The abundant precipitation of
634 massive magnetites in mesh cores would explain the formation of serpentine with
635 higher Mg# in response to changes in the conditions of hydrothermal alteration. It
636 should be noted that the marked crystallization of magnetite in mesh cores could be a
637 consequence of the combined variation in fluid temperature and $\delta^{18}O$ composition,
638 water/rock ratio (W/R) and redox conditions (Klein et al., 2009, 2013).
639 In light of the above assumptions, the physical-chemical conditions at which the
640 serpentine-magnetite pairs in mesh textures formed (i.e., T = 204 to 132 °C and
641 $\delta^{18}O_{(water)}$ = 5 to 2‰) can be considered valid for serpentine in all mesh cores. It is
642 worth noting that the concomitance between cooling and decrease in water $\delta^{18}O$
643 values results in a net variation of magnetite and serpentine $\delta^{18}O$ values by ~5.5‰
644 and ~0.4‰, respectively (Fig. A.7); this is consistent with the variability in $\delta^{18}O$
645 values measured by SIMS in serpentine-magnetite pairs (Table 1). The decrease in
646 fluid $\delta^{18}O$ values during cooling is consistent with a progressive evolution from a
647 rock-dominated system during early stages of serpentinization (or low W/R), with
648 water $\delta^{18}O$ values similar to the oxygen isotopic composition of the upper mantle
649 ($\delta^{18}O_{mantle}$ = 5.5‰, $\delta^{18}O_{olivine}$ = 5.18±0.28‰; e.g., Mattey et al., 1994; Chazot et al.,
650 1997), to a fluid-dominated system during later stages of serpentinization (or high

651 W/R) and exhumation of the mantle near the seafloor. Calculated water $\delta^{18}O$ values of
652 ~2‰ agree well with $\delta^{18}O$ values of 1.2-1.5‰ (Logatchev hydrothermal field) and
653 2.2-2.4‰ (Nibelungen hydrothermal field) measured in hot (T = 192-365°C)
654 ultramafic-hosted vent fluids sampled along the Mid-Atlantic slow-spreading ridge
655 (e.g., Charlou et al., 2010 and references therein; Schmidt et al., 2011), which are
656 higher in $\delta^{18}O$ than present-day pure seawater (0‰) due to interaction with the
657 oceanic crust (e.g., Mével, 2003). Similar temperatures (T = 265-364°C) and $\delta^{18}O$
658 values (1.1-2.4‰) are also recorded in mafic-hosted vent fluids (e.g., Jean-Baptiste et
659 al., 1997).

660 Our new *in situ* data are overall in agreement with the original suggestion of Lafay
661 et al. (2017) who, in continuity with the tectonic models proposed by Manatschal et
662 al. (2011), proposed that exhumation of oceanic units occurred along detachment
663 faults favoring hydration and carbonation of mantle rocks (Fig. 12a). The authors
664 proposed that serpentinization initiated in a shallow seafloor environment at
665 conditions of at least 150 °C, with reactive fluids assumed to have $\delta^{18}O$ values of 0-
666 2‰. The new *in situ* data suggest comparable temperature estimates within
667 uncertainty, but independently constrain the composition and origin of the interacting
668 fluids as well as identify that early serpentinization was followed by early low-
669 temperature carbonation due to exposure of the mantle rocks on the paleo seafloor and
670 interaction with low-temperature seawater (Fig. 12a). This is documented by the
671 zonation in $\delta^{18}O$ values observed in some carbonate generations (Fig. 7, 10), with
672 texturally older calcite domains having high $\delta^{18}O$ values in zoned C2 calcite mesh
673 (18.0-30.6‰), at the edges of zoned C1 veins (18.7-22.3‰) and in the cores of zoned
674 C1' domains (18.2-24.9‰), which are comparable to those reported for marine
675 carbonates and metacarbonates from the Lago Nero unit (Lemoine et al., 1983). Such

carbonates likely formed at temperatures as low as 10 °C assuming interaction with pure seawater in an ice-free world ($\delta^{18}O$ = –1‰). Such low carbonation temperatures relative to serpentinization are also consistent with the observation that calcite in mesh textures is clearly replacing (hence postdating) serpentine.

5.2.2. An active hydrothermal cell: coupled high-*T* carbonation and serpentinization

An overall decrease in oxygen isotope values with textural progression is recorded by both serpentine and carbonate in all investigated samples (Fig. 6, 7, 10). In particular, $\delta^{18}O$ values of serpentine in V-2 veins ($\delta^{18}O$ = 3.2-4.2‰) and hourglass textures ($\delta^{18}O$ = 3.8-5.7‰) are ~3‰ lower on average relative to serpentine in mesh cores (Fig. 6). Similarly, texturally younger calcite in zoned C2 mesh, C1 veins and C1' domains has $\delta^{18}O$ values down to ~10‰ (Fig. 7, 10). Low oxygen isotope ratios are also recorded in lizardite at the boundary between serpentinite clast and carbonate matrix ($\delta^{18}O$ = 3.1-5.4‰), chrysotile intergrown with fine-grained C3 calcite ($\delta^{18}O$ = 3.0-5.7‰), C3 calcite matrix ($\delta^{18}O$ = 9.8-12.8‰), C3-veins ($\delta^{18}O$ = 10.7-11.4‰) and C1'-veins ($\delta^{18}O$ = 10.9‰). Oxygen isotope thermometry from mineral pairs (see above) suggests that such a drop in $\delta^{18}O$ values in both serpentine and carbonates is consistent with a crystallization temperature of up to 240 °C and water $\delta^{18}O$ value of 2±1‰. The smooth oxygen isotope zoning in both C1 veins and C1' domains as well as the similarity in fluid $\delta^{18}O$ compositions between early and late stages of hydrothermal alteration point to a continuous process that likely occurred entirely in a seafloor environmental setting. The pervasive carbonation textures often overprint serpentinization ones, but we do not exclude that carbonation initiated while residual

anhydrous silicates were still present. The calculated oxygen isotope compositions of water are consistent with isotopically shifted seawater rather than indicative of interaction with meteoric water or metamorphic fluids in continental settings. Oxygen isotope values measured in serpentine fall in the range of oceanic serpentinites (Wenner and Taylor, 1973) and all values of $\delta^{13}C$ in carbonates (from –2.6 to +2.4‰) suggest a seawater origin for carbon. It is worth noting that in a $\delta^{18}O$ versus $\delta^{13}C$ plot, the carbonates from the Chenaillet ophiolite show a distinct horizontal trend parallel to the $\delta^{18}O$ axis (Fig. A.5) suggesting that the fraction of CO_2 in the fluid was not significant. Calcite can precipitate at a mole fraction of $CO_2/(CO_2 + H_2O)$ as low as 0.01, but in such case a high water/rock ratio is required for a significant carbonation. Carbonate cements commonly form at low temperature from seawater (biogenic and abiogenic) and freshwater (calcretes and speleothems). High-$\delta^{18}O$ carbonates are assumed to form in equilibrium with very low-*T* seawater and our new thermometry estimates suggest that low-$\delta^{18}O$ carbonates in the Chenaillet ophicarbonates formed at high temperature. Consequently, both temperature and water $\delta^{18}O$ must have changed. The flat trend can result from the dissolution and reprecipitation of pre-existing carbonates that interacted with nearly pure water such that the $\delta^{13}C$ remained constant. This agrees with observations of dissolution and reprecipitation textures in the carbonates of the investigated samples.

Heating associated with burial during oceanic spreading is an unlikely scenario to explain this high-*T* hydrothermal event due to the intense fracturing of the ophicarbonates that points to active tectonics, accordingly to Lafay et al. (2017) who also suggested that authigenic carbonation, partially replacing serpentinites and achieving mantle minerals alteration, occurred under brittle conditions favored by the likely fluid-dominated system and tectonic context. In fact, the authors hypothesized

726 that the composition of the fluid and the temperature conditions evolved in a
727 hydrothermal environment comparable to that observed in the vicinity of mid-ocean
728 hydrothermal vents, i.e. active tectonic and magmatic conditions. The occurrence of a
729 warmer (200-240 °C) stage of hydrothermal alteration due to interaction with evolved
730 seawater-derived fluids ($\delta^{18}O$ = 2-3‰) documented by the new *in situ* data could be
731 the result of burial by lavas causing reheating and channeling of upwelling
732 hydrothermal fluids along high-angle faults (Fig. 12b). Such a scenario would be
733 consistent with the tectonic models of Manatschal et al. (2011) for the Chenaillet
734 ophiolite suggesting that a first stage of mantle exhumation along a detachment fault
735 was followed by a stage of 'high-angle extrusion', when magma and fluids were
736 remobilized along high-angle faults acting also as feeder channels for the overlying
737 pillow basalts. A similar model of high-temperature hydrothermal discharge, driven
738 by mafic intrusions, along normal faults lying at high angle to an oceanic detachment
739 surface was proposed by Alt et al. (2018) in the northern Appenine ophiolites. The
740 authors documented an evolution of the fault system at the paleo-seafloor from talc
741 alteration and sulfide deposits, typical of high-temperature hydrothermal discharge (T
742 ≈ 350 °C), to carbonated serpentinites formed at T ≈ 100 °C (Alt et al., 2018).
743 Carbonates formed at temperatures as high as ~ 225 °C are observed also in the
744 serpentinite basement of the Lost City Hydrothermal Field in the Mid-Atlantic Ridge,
745 where they precipitate from warm hydrothermal fluids with high concentrations of
746 methane and hydrogen derived from serpentinization (Früh-Green et al., 2003).
747
748 **5.2.3. Late stage veining**
749

750 The youngest C4 calcite vein records a large variability in $\delta^{18}O$ values (12.3 to
751 23.9‰) and the highest average oxygen isotope composition among different
752 carbonate generations (Fig. 7). No independent calculations of temperature and fluid
753 oxygen isotope composition are possible due to the lack of mineral pairs. It is,
754 therefore, necessary to assume that the variation in $\delta^{18}O$ values is due to a variation in
755 temperature, fluid oxygen isotope composition or more likely a combination of both.
756 Given the lowest $\delta^{18}O$ values are comparable to those measured in the "high-
757 temperature" carbonates, it is plausible that formation of the C4 vein started in similar
758 physical-chemical conditions and continued due to interaction with progressively
759 cooler and low- $\delta^{18}O$ hydrothermal fluids (down to a minimum of ~40 °C, assuming
760 $\delta^{18}O_{(water)}$ of –1‰) due to mixing with fresh seawater channeled along fractures at
761 shallower depths. Such estimates are comparable, for instance, to the active vent
762 fluids sampled at the Lost City Hydrothermal Field characterized by low temperature
763 (T = 55-75 °C) and $\delta^{18}O$ values (0-0.1‰), and are interpreted to result from mixing
764 between seawater and high-pH fluids derived from subsurface serpentinization
765 reactions (Früh-Green et al., 2003). The evolutionary model suggested here for the
766 hydrothermal alteration of the Chenaillet ophicarbonates is consistent with the overall
767 observation that this ophiolitic terrain was only partly affected by low-grade
768 metamorphism during obduction.
769
770 **6. CONCLUSIONS**
771
772 We performed *in situ* analysis by SIMS of oxygen and carbon isotopes in
773 serpentine, calcite, dolomite and magnetite from ophicarbonate samples from the
774 Chenaillet ophiolitic complex (western Alps). SIMS analysis revealed unprecedented

775 zoning in oxygen isotope ratios of serpentine (3.0 to 8.8‰), calcite (9.4 to 30.6‰)
776 and magnetite (–5.0 to –10.6‰) relative to previous studies, which relied on
777 conventional bulk analysis. To the best of our knowledge, we document the first
778 evidence of 'cold carbonates' (i.e., carbonates with $\delta^{18}O > 25‰$; e.g., Fig. 6 in Picazo
779 et al., 2020 and references therein) in Alpine ophiolites. The lack of such high oxygen
780 isotope signatures in other Alpine ophiolitic terrains could be due to the much larger
781 sampling scale of the bulk techniques that average $\delta^{18}O$ values of multiple mineral
782 generations. The high spatial resolution of SIMS allowed direct quantification of
783 oxygen isotope ratios in mineral pairs that are in textural equilibrium and are
784 interpreted to have co-crystallized. The relative oxygen isotope homogeneity of the
785 targeted mineral pairs is consistent with isotopic equilibrium allowing for the
786 independent calculation of equilibrium temperatures and water oxygen isotope values.
787 Considering that the temperature-pressure stabilities of serpentine minerals are not
788 well constrained, *in situ* stable isotope thermometry presents a powerful tool to
789 constrain the conditions at which alteration of ultramafic rocks occurs in various
790 tectonic settings. Additionally, numerical models by Klein and Garrido (2011) show
791 that temperature-dependent activity gradients of both aqueous carbon dioxide
792 (aCO_2,aq) and aqueous silica ($aSiO_2$,aq) determine the carbonation potential of
793 serpentinite. Independently constraining the formation temperature is therefore
794 essential to estimating $aSiO_{2(aq)}$, $aCO_{2(aq)}$, oxygen fugacity and pH, which in turn
795 would allow estimating the phase equilibria with implications for the monitoring of
796 reaction progress during CO_2 sequestration of ultramafic rocks (Klein and Garrido,
797 2011). Nevertheless, a major source of uncertainty on the calculation of alteration
798 temperatures, particularly for the serpentine-water system, remains the large
799 discrepancy between different calibrations of the oxygen isotope fractionation at $T <$

200 °C, hence future studies should aim to improve such calibrations. The new dataset and thermometry estimates in the Chenaillet ophiolite are interpreted as indicative of a continuous hydrothermal alteration starting during uplift and exposure of the lithospheric mantle to the seafloor, subsequently followed by further carbonation and serpentinization induced by hot (up to 240 °C) and isotopically shifted ($\delta^{18}O$ ~2‰) seawater, and finally by channeling of and mixing with low-*T* and low-$\delta^{18}O$ seawater along fractures. This scenario is consistent with alteration occurring in long-lived hydrothermal systems controlled by tectonic activity where multiple metasomatic events can explain effective mantle hydration and carbonation over a few tens of thousands of years. Carbonation of ultramafic rocks in oceanic settings plays an important role for the global carbon cycle as abyssal peridotites and serpentinites might act as a sink for CO_2. Unraveling the complexity and sequence of reactions, temperatures and fluid compositions responsible for peridotite or serpentinite carbonation in oceanic and continental settings is important for correctly estimating rates of mineral carbonation and potential for CO_2 intake.

ACKNOWLEDGEMENTS

We thank Mike Spicuzza and Brian Hess for assistance with sample preparation, Bil Schneider and John Fournelle for assistance with SEM and EPMA analyses, Kouki Kitajima for assistance in the SIMS lab and data processing. We are grateful to Eugenio Piluso for fruitful discussions and for reading an earlier version of the manuscript. Jeffrey Alt, Frieder Klein and an anonymous reviewer are acknowledged for constructive reviews that helped improve the manuscript. We also thank Frieder Klein for editorial handling. This work is supported by the U.S.

825 Department of Energy, Office of Science, Office of Basic Energy Sciences
826 (Geosciences) under Awards Number DE-FG02-93ER14389 and DE-SC0020666.
827 WiscSIMS is supported by the U.S. National Science Foundation (EAR-1658823, -
828 2004618) and the University of Wisconsin- Madison.

829 **REFERENCES**

830

831 Agrinier P. and Cannat M. (1997) Oxygen-isotope constraints on serpentinization
832 processes in ultramafic rocks from the mid-atlantic ridge (23°N). *Proc. Ocean*
833 *Drill. Program, Sci. Results* **153**, 381–388.
834 doi:10.2973/odp.proc.sr.153.033.1997

835 Agrinier P. and Javoy M. (2016) Unbiased isotope equilibrium factors from partial
836 isotope exchange experiments in 3-exchange site systems. *Geochim. Cosmochim.*
837 *Acta* **189**, 197–213.

838 Allen D. E and Seyfried W. E. (2003) Compositional controls on vent fluids from
839 ultramafic-hosted hydrothermal systems at mid-ocean ridges: An experimental
840 study at 400 °C, 500 bars. *Geochim. Cosmochim. Acta* **67**, 1531–1542.

841 Alt J. C. and Shanks W. C. (2006) Stable isotope compositions of serpentinite
842 seamounts in the Mariana forearc: Serpentinization processes, fluid sources and
843 sulfur metasomatism. *Earth Planet. Sci. Lett.* **242**, 272–285.
844 doi:10.1016/j.epsl.2005.11.063

845 Alt J. C., Garrido C. J., Shanks W. C., Turchyn A., Padrón-Navarta J. A., López
846 Sánchez-Vizcaíno V., Gómez Pugnaire M. T. and Marchesi C. (2012) Recycling
847 of water, carbon, and sulfur during subduction of serpentinites: A stable isotope
848 study of Cerro del Almirez, Spain. *Earth Planet. Sci. Lett*. **327–328**, 50–60.
849 doi:10.1016/j.epsl.2012.01.029

850 Alt J., Crispini L., Gaggero L., Levine D., Lavagnino G., Shanks P. and Gulbransen
851 C. (2018) Normal faulting and evolution of fluid discharge in a Jurassic seafloor
852 ultramafic-hosted hydrothermal system. *Geology* **46**, 523–526.

853 Andreani M., Mével C., Boullier A. M. and Escartín J. (2007) Dynamic control on

854 serpentine crystallization in veins: Constraints on hydration processes in oceanic
855 peridotites. *Geochemistry, Geophys. Geosystems* **8**, doi:10.1029/2006GC001373
856 Bach W., Rosner M., Jöns N., Rausch S., Robinson L. F., Paulick H. and Erzinger J.
857 (2011) Carbonate veins trace seawater circulation during exhumation and uplift
858 of mantle rock: Results from ODP Leg 209. *Earth Planet. Sci. Lett.* **311**, 242–
859 252. doi:10.1016/j.epsl.2011.09.021
860 Barnes I. and O'Neil J. R. (1969) The relationship between fluids in some fresh
861 Alpine-type ultramafics and possible modern serpentinization, Western United
862 States. *Geol. Soc. Am. Bull*. **80**, 1947–1960.
863 Barnes I., O'Neil J. R. and Trescases J. J. (1978) Present day serpentinization in New
864 Caledonia, Oman and Yugoslavia. *Geochim. Cosmochim. Acta* **42**, 144–145.
865 Barnes J. D., Paulick H., Sharp Z. D., Bach W. and Beaudoin G. (2009) Stable isotope
866 ($\delta^{18}O$, δD, $\delta^{37}Cl$) evidence for multiple fluid histories in mid-Atlantic abyssal
867 peridotites (ODP Leg 209). *Lithos* **110**, 83–94. doi:10.1016/j.lithos.2008.12.004
868 Barnes J. D., Eldam R., Lee C.-T. A., Errico J. C., Loewy S. and Cisneros M. (2013)
869 Petrogenesis of serpentinites from the Franciscan Complex, western California,
870 USA. *Lithos* **178**, 143–157. doi:10.1016/j.lithos.2012.12.018
871 Boillot G., Féraud G., Recq M. and Girardeau J. (1989) Undercrusting by serpentinite
872 beneath rifted margings. *Nature* **341**, 523–525.
873 Bonatti E., Emiliani C., Ferrara G., Honnorez J. and Rydell H. (1974) Ultramafic-
874 carbonate breccias from the equatorial mid atlantic ridge. *Mar. Geol*. **16**, 83–102.
875 Bottinga Y. and Javoy M. (1973) Comments on oxygen isotope geothermometry.
876 *Earth Planet. Sci. Lett.* **20**, 250–265.
877 Boudier F., Baronnet A. and Mainprice D. (2010) Serpentine Mineral Replacements
878 of Natural Olivine and their Seismic Implications: Oceanic Lizardite versus

879 Subduction-Related Antigorite. *J. Petrol.* **51**, 495–512.
880 doi:10.1093/petrology/egp049
881 Charlou J. L., Donval J. P., Konn C., Ondréas H. and Fouquet Y. (2010) High
882 production and fluxes of H_2 and CH_4 and evidence of abiotic hydrocarbon
883 synthesis by serpentinization in ultramafic-hosted hydrothermal systems on the
884 Mid-Atlantic Ridge. In *Diversity of hydrothermal systems on slow spreading*
885 *ocean ridges* (eds. P. A. Rona, C. W. Devey, J. Dyment and B. J. Murton),
886 *American Geophysical Union* **188**, 265–296.
887 Chazot G., Lowry D., Menzies M. and Mattey D. (1997) Oxygen isotopic
888 composition of hydrous and anhydrous mantle peridotites. *Geochim.*
889 *Cosmochim. Acta* **61**, 161–169.
890 Collins N. C., Bebout G. E., Angiboust S., Agard P., Scambelluri M., Crispini L. and
891 John T. (2015) Subduction zone metamorphic pathway for deep carbon cycling:
892 II. Evidence from HP/UHP metabasaltic rocks and ophicarbonates. *Chem. Geol*.
893 **412**, 132–150. doi:10.1016/j.chemgeo.2015.06.012
894 de Obeso J. C. and Kelemen P. B. (2018) Fluid rock interactions on residual mantle
895 peridotites overlain by shallow oceanic limestones: Insights from Wadi Fins,
896 Sultanate of Oman. *Chem. Geol*. **498**, 139–149.
897 doi:10.1016/j.chemgeo.2018.09.022
898 Deschamps F., Godard M., Guillot S. and Hattori K. (2013) Geochemistry of
899 subduction zone serpentinites: A review. *Lithos* **178**, 96–127.
900 doi:10.1016/j.lithos.2013.05.019
901 Dilek Y. and Furnes H. (2014) Ophiolites and their origins. *Elements* **10**, 93–100.
902 Falk E. S. and Kelemen P. B. (2015) Geochemistry and petrology of listvenite in the
903 Samail ophiolite, Sultanate of Oman: Complete carbonation of peridotite during

ophiolite emplacement. *Geochim. Cosmochim. Acta* **160**, 70–90. doi:10.1016/j.gca.2015.03.014

Falk E. S., Guo W., Paukert A. N., Matter J. M., Mervine E. M. and Kelemen P. B. (2016) Controls on the stable isotope compositions of travertine from hyperalkaline springs in Oman: Insights from clumped isotope measurements. *Geochim. Cosmochim. Acta* **192**, 1–28. doi:10.1016/j.gca.2016.06.026

Früh-Green G. L., Weissert H. and Bernoulli D. (1990) A multiple fluid history recorded in Alpine ophiolites. *J. Geol. Soc. London* **147**, 959–970. doi:10.1144/gsjgs.147.6.0959

Früh-Green G. L., Plas A. and Lecuyer C. (1996) Petrologic and Stable Isotope Constraints on Hydrothermal Alteration and Serpentinization of the EPR Shallow Mantle at Hess Deep (Site 895). *Proc. Ocean Drill. Program, 147 Sci. Results* **147**, doi:10.2973/odp.proc.sr.147.016.1996

Früh-Green G. L., Connolly J. A. D., Plas A., Kelley D. S. and Grobety B. (2004) Serpentinization of the oceanic peridotites: Implication for geochemical cycles and biological activity. *Geophys. Monogr. Ser.* **144**, 119–136.

Goffé B., Schwartz S., Lardeaux J. M. and Bousquet R. (2004) Metamorphic structure of the Western and Ligurian Alps. *Mitt. Osterr. Miner. Ges*. **149**, 125–144.

Golyshev S. I., Padalko N. I. and Pechenkin S. A. (1981) Fractionation of stable isotopes in carbonate systems. *Geochem. Int'l.* **10**, 85–99.

Huberty J. M., Kita N. T., Kozdon R., Heck P. R., Fournelle J. H., Spicuzza M. J., Xu H. and Valley J. W. (2010) Crystal orientation effects in $\delta^{18}O$ for magnetite and hematite by SIMS. *Chem. Geol*. **276**, 269–283.

Jean-Baptiste P., Charlou J. L. and Stievenard M. (1997) Oxygen isotope study of mid-ocean ridge hydrothermal fluids: Implication for the oxygen-18 budget of

the oceans. *Geochim. Cosmochim. Acta* **61**, 2669–2677.

Kelemen P. B. and Matter J. (2008) In situ carbonation of peridotite for CO_2 storage. *Proc. Natl. Acad. Sci.* **105**, 17295–17300.

Kelemen P. B., Matter J., Streit E. E., Rudge J. F., Curry W. B. and Blusztajn J. (2011) Rates and Mechanisms of Mineral Carbonation in Peridotite: Natural Processes and Recipes for Enhanced, in situ CO_2 Capture and Storage. *Annu. Rev. Earth Planet. Sci*. **39**, 545–576. doi:10.1146/annurev-earth-092010-152509

Kelley D. S., Karson J. A., Früh-Green G. L., Yoerger D. R., Shank T. M., Butterfield D. A., Hayes J. M., Schrenk M. O., Olson E. J., Proskurowski G., Jakuba M., Bradley A., Larson B., Ludwig K., Glickson D., Buckman K., Bradley A. S., Brazelton W. J., Roe K., Bernasconi S. M., Elend M. J., Lilley M. D., Baross J. A., Summons R. E. and Sylva S. P. (2005) A Serpentinite-Hosted Ecosystem: The Lost City Hydrothermal Field. *Science* **307**, 1428–1435.

Kelly J. L., Fu B., Kita N. T. and Valley J. W. (2007) Optically continuous silcrete quartz cements of the St. Peter Sandstone: High precision oxygen isotope analysis by ion microprobe. *Geochim. Cosmochim. Acta* **71**, 3812–3832. doi:10.1016/j.gca.2007.05.014

Kim S.-T. and O'Neil J. R. (1997) Equilibrium and nonequilibrium oxygen isotope effects in synthetic carbonates. *Geochim. Cosmochim. Acta* **61**, 3461–3475.

Kita N. T., Huberty J. M., Kozdon R., Beard B. L. and Valley J. W. (2011) High precision SIMS oxygen, sulfur and iron stable isotope analyses of geological materials: Accuracy, surface topography and crystal orientation. SIMS XVII Proceedings, *Surface and Interface Analysis* **43**, 427-431, DOI 10.1002/sia.3424.

Klein F. and Garrido C. J. (2011) Thermodynamic constraints on mineral carbonation of serpentinized peridotite. *Lithos* **126**, 147–160.

954 Klein F., Bach W., Jöns N., McCollom T., Moskowitz B. and Berquó T. (2009) Iron
955 partitioning and hydrogen generation during serpentinization of abyssal
956 peridotites from 15 N on the Mid-Atlantic Ridge. *Geochim. Cosmochim. Acta*
957 **73(22)**, 6868–6893.
958 Klein F., Bach W. and McCollom T. M. (2013) Compositional controls on hydrogen
959 generation during serpentinization of ultramafic rocks. *Lithos* **178**, 55–69.
960 Kozdon R., Ushikubo T., Kita N. T., Spicuzza M. and Valley J. W. (2009) Intratest
961 oxygen isotope variability in the planktonic foraminifer N. pachyderma: Real vs.
962 apparent vital effects by ion microprobe. *Chem. Geol.* **258**, 327–337.
963 doi:10.1016/j.chemgeo.2008.10.032
964 Lafay R., Baumgartner L. P., Schwartz S., Picazo S., Montes-Hernandez G. and
965 Vennemann T. (2017) Petrologic and stable isotopic studies of a fossil
966 hydrothermal system in ultramafic environment (Chenaillet ophicalcites,
967 Western Alps, France): Processes of carbonate cementation. *Lithos* **294–295**,
968 319–338. doi:10.1016/j.lithos.2017.10.006
969 Lafay R., Baumgartner L. P., Putlitz B. and Siron G. (2019) Oxygen isotope
970 disequilibrium during serpentinite dehydration. *Terra Nov*. **31**, 94–101.
971 doi:10.1111/ter.12373
972 Lagabrielle Y. and Cannat M. (1990) Alpine Jurassic ophiolites resemble the modern
973 central Atlantic basement. *Geology* **18**, 319–322.
974 Lagabrielle Y. and Lemoine M. (1997) Alpine, Corsican and Apennine ophiolites: the
975 slow-spreading ridge model. *C. R. Acad. Sci. Ser. IIA Earth Planet. Sci*. **325**,
976 909–920.
977 Lemoine M., Bourbon M., Graciansky P.-C. and Létolle R. (1983) Isotopes du
978 carbone et de l'oxygène de calcaires asociés à des ophiolites (Alpes Occidentales,

979 Corse, Apennin): indices possibles d'un hydrothermalisme océanique téthusien.
980 *Revue de Géologie Dynamique et de Géographie Physiqie* **24**, 305–314.
981 Li X.-H., Faure M., Lin W. and Manatschal G. (2013) New isotopic constraints on
982 age and magma genesis of an embryonic oceanic crust: The Chenaillet Ophiolite
983 in the Western Alps. *Lithos* **160–161**, 283–291. doi:10.1016/j.lithos.2012.12.016
984 Manatschal G. and Müntener O. (2009) A type sequence across an ancient magma-
985 poor ocean-continent transition: the example of the western Alpine Tethys
986 ophiolites. *Tectonophysics* **473**, 4–19. doi:10.1016/j.tecto.2008.07.021
987 Manatschal G., Sauter D., Karpoff A. M., Masini E., Mohn G. and Lagabrielle Y.
988 (2011) The Chenaillet Ophiolite in the French/Italian Alps: An ancient analogue
989 for an Oceanic Core Complex? *Lithos* **124**, 169–184.
990 doi:10.1016/j.lithos.2010.10.017
991 Martin B. and Fyfe W. S. (1970) Some experimental and theoretical observations on
992 the kinetics of hydration reactions with particular reference to serpentinization.
993 *Chem. Geol*. **6**, 185–202.
994 Mattey D., Lowry D. and Macpherson C. (1994) Oxygen isotope composition of the
995 mantle peridotite. *Earth Planet. Sci. Lett.* **128**, 231–241.
996 Matthews A. and Katz A. (1977) Oxygen isotope fractionation during the
997 dolomitization of calcium carbonate. *Geochim. Cosmochim. Acta* **41**, 1431–
998 1438.
999 Mével C. (2003) Serpentinization of abyssal peridotites at mid-ocean ridges. *C. R.*
1000 *Geosci*. **335**, 825–852. doi:10.1016/j.crte.2003.08.006
1001 Mével C., Caby R. and Kienast J.-R. (1978) Amphibolite facies conditions in the
1002 oceanic crust: example of amphibolitized flaser-gabbro and amphibolites from
1003 the Chenaillet ophiolite massif (Hautes Alpes, France). *Earth Planet. Sci. Lett.*

39, 98–108.

Miller H. M., Matter J. M., Kelemen P., Ellison E. T., Conrad M. E., Fierer N., Ruchala T., Tominaga M. and Templeton A. S. (2016) Modern water/rock reactions in Oman hyperalkaline peridotite aquifers and implications for microbial habitability. *Geochim. Cosmochim. Acta* **179**, 217–241. doi:10.1016/j.gca.2016.01.033

Neal C. and Stanger G. (1985) Past and present serpentinisation of ultramafic rocks; an example from the Semail ophiolite nappe of northern Oman. In *The Chemistry of Weathering* (eds. J. I. Drewer). D. Reidel Publishing Company, Holland, pp. 249–275.

Noël J., Godard M., Oliot E., Martinez I., Williams M., Boudier F., Rodriguez O., Chaduteau C., Escario S. and Gouze P. (2018) Evidence of polygenetic carbon trapping in the Oman Ophiolite: Petro-structural, geochemical, and carbon and oxygen isotope study of the Wadi Dima harzburgite-hosted carbonates (Wadi Tayin massif, Sultanate of Oman). *Lithos* doi:10.1016/j.lithos.2018.08.020

Northrop D. A. and Clayton R. N. (1966) Oxygen isotope fractionations in systems containing dolomite. *J. Geol*. **74**, 174–196.

O'Hanley D. S. and Offler R. (1992) Characterization of multiple serpentinization, Woodsreef, New South Wales. *Can. Mineral.* **30**, 1113–1126.

O'Neil J. R., Clayton R. N. and Mayeda T. K. (1969) Oxygen Isotope Fractionation in Divalent Metal Carbonates. *J. Chem. Phys*. **51**, 5547–5558.

Pearce J. A. (2014) Immobile element fingerprinting of ophiolites. *Elements* **10**, 101–108.

Picazo S., Lafay R., Faucheux V. and Vennemann T. (2019) New constraints on carbonation associated with brecciation in hyperextended margins (example of

1029 Iberia and Newfoundland margins). *Terra Nov*. **31**, 317–331.
1030 doi:10.1111/ter.12383
1031 Picazo S., Malvoisin B., Baumgartner L. and Bouvier Anne-Sophie (2020) Low
1032 temperature serpentinite replacement by carbonates during seawater influx in the
1033 Newfoundland Margin. *Minerals* **10**, 184. doi:10.3390/min10020184
1034 Rouméjon S., Williams M. J. and Früh-Green G. L. (2018). In-situ oxygen isotope
1035 analyses in serpentine minerals: Constraints on serpentinization during tectonic
1036 exhumation at slow- and ultraslow-spreading ridges. *Lithos* **323**, 156–173.
1037 doi:10.1016/j.lithos.2018.09.021
1038 Saccocia P. J., Seewald J. S. and Shanks W. C. (2009) Oxygen and hydrogen isotope
1039 fractionation in serpentine-water and talc-water systems from 250 to 450 °C, 50
1040 MPa. *Geochim. Cosmochim. Acta* **73**, 6789–6804. doi:10.1016/j.gca.2009.07.036
1041 Savin S. M. and Lee M. (1988) Isotopic studies of phyllosilicates. *Rev. Mineral.* **19**,
1042 189–223.
1043 Scambelluri M., Fiebig J., Malaspina N., Müntener O. and Pettke T. (2004)
1044 Serpentinite Subduction: Implications for Fluid Processes and Trace-Element
1045 Recycling. *Int. Geol. Rev*. **46**, 595–613. doi:10.2747/0020-6814.46.7.595
1046 Schmidt K., Garbe-Schönberg D., Koschinsky A., Straus H., Jost C. L., Klevenz V.
1047 and Königer P. (2011) Fluid elemental and stable isotope composition of the
1048 Nibelungen hydrothermal field (8°18'S, Mid-Atlantic Ridge): Constraints on
1049 fluid-rock interaction in heterogeneous lithosphere. *Chem. Geol.* **280**, 1–18.
1050 Schwarzenbach E. M., Früh-Green G. L., Bernasconi S. M., Alt J. C. and Plas A.
1051 (2013) Serpentinization and carbon sequestration: A study of two ancient
1052 peridotite-hosted hydrothermal systems. *Chem. Geol.* **351**, 115–133.
1053 doi:10.1016/j.chemgeo.2013.05.016

1054 Scicchitano M. R., Rubatto D., Hermann J., Shen T., Padrón-Navarta J. A., Williams
1055 I. S. and Zheng Y.-F. (2018a) In Situ Oxygen Isotope Determination in
1056 Serpentine Minerals by Ion Microprobe: Reference Materials and Applications to
1057 Ultrahigh-Pressure Serpentinites. *Geostand. Geoanalytical Res*. **42**, 459–479.
1058 doi:10.1111/ggr.12232
1059 Scicchitano M. R., Rubatto D., Hermann J., Majumdar A. S. and Putnis A. (2018b)
1060 Oxygen isotope analysis of olivine by ion microprobe: Matrix effects and
1061 applications to a serpentinised dunite. *Chem. Geol*. **499**, 126–137.
1062 doi:10.1016/j.chemgeo.2018.09.020
1063 Scicchitano M. R., Spicuzza M. J., Ellison E. T., Tuschel D., Templeton A. S. and
1064 Valley J. W. (2020) In situ oxygen isotope determination in serpentine minerals
1065 by SIMS: Addressing matrix effects and providing new insights on
1066 serpentinisation at Hole BA1B (Samail ophiolite, Oman). *Geostand.*
1067 *Geoanalytical Res*. **45**, 161-187. doi: 10.1111/ggr.12359
1068 Skelton A. D. L. and Valley J. W. (2000) The relative timing of serpentinisation and
1069 mantle exhumation at the ocean-continent transition, Iberia: Constraints from
1070 oxygen isotopes. *Earth Planet. Sci. Lett*. **178**, 327–338. doi:10.1016/S0012-
1071 821X(00)00087-X
1072 Śliwiński M. G., Kitajima K., Kozdon R., Spicuzza M. J., Fournelle J. H., Denny A.
1073 and Valley J. W. (2015a) Secondary Ion Mass Spectrometry Bias on Isotope
1074 Ratios in Dolomite–Ankerite, Part I: $\delta^{18}O$ Matrix Effects. *Geostand.*
1075 *Geoanalytical Res*. **40**, 157–172. doi:10.1111/j.1751-908X.2015.00364.x
1076 Śliwiński M. G., Kitajima K., Kozdon R., Spicuzza M. J., Fournelle J. H., Denny A.
1077 and Valley J. W. (2015b) Secondary Ion Mass Spectrometry Bias on Isotope
1078 Ratios in Dolomite–Ankerite, Part II: $\delta^{13}C$ Matrix Effects. *Geostand.*

Geoanalytical Res. **40**, 173–184. doi:10.1111/j.1751-908X.2015.00380.x

Staudigel H., Furnes H. and Smits M. (2014) Deep biosphere record of in situ oceanic lithosphere and ophiolites. *Elements* **10**, 121–126.

Streit E., Kelemen P. and Eiler J. (2012) Coexisting serpentine and quartz from carbonate-bearing serpentinized peridotite in the Samail Ophiolite, Oman. *Contrib. to Mineral. Petrol*. **164,** 821-837. doi:10.1007/s00410-012-0775-z

Turnier R. B., Katzir Y., Kitajima K., Orland I. J., Spicuzza M. J. and Valley J. W. (2020) Calibration of oxygen isotope fractionation and calcite-corundum thermometry in emery at Naxos, Greece. *J. Metamorph. Geol*. **38**, 53–70.

Valley J. W. and Kita N. T. (2009) In situ oxygen isotope geochemistry by ion microprobe. *Mineral. Assoc. Canada Short Course Ser*. **41**, 19–63.

Vitale Brovarone A., Martinez I., Elmaleh A., Compagnoni R., Chaduteau C., Ferraris C. and Esteve I. (2017) Massive production of abiotic methane during subduction evidenced in metamorphosed ophicarbonates from the Italian Alps. *Nat. Commun*. **8**, 1–13. doi:10.1038/ncomms14134

Wenner D. B. and Taylor H. P. (1971) Temperatures of serpentinization of ultramafic rocks based on O^{18}/O^{16} fractionation between coexisting serpentine and magnetite. *Contrib. to Mineral. Petrol*. **32**, 165–185. doi:10.1007/BF00643332

Wenner D. B. and Taylor H. P. (1973) Oxygen and hydrogen isotope studies of the serpentinization of ultramafic rocks in oceanic environments and continental ophiolite complexes. *Am. J. Sci.* **273***,* 207-239. doi:10.2475/ajs.273.3.207

Zheng Y.-F. (1991) Calculation of oxygen isotope fractionation in metal oxides. *Geochim. Cosmochim. Acta* **55**, 2299–2307.

Zheng Y.-F. (1993) Calculation of oxygen isotope fractionation in hydroxyl-bearing silicates. *Earth Planet. Sci. Letters* **120**, 247–263.

1104 Zheng Y.-F., Metz P., Satir M. and Sharp Z. D. (1994) An experimental calibration of
1105 oxygen isotope fractionation between calcite and forsterite in the presence of a
1106 CO_2-H_2O fluid. *Chem. Geol*. **116**, 17–27.
1107
1108

FIGURE AND TABLE CAPTIONS

Fig. 1. (a) Tectonic map of the Piemont domain of the western Alps. (b). Geological map of the Chenaillet massif (star in Fig 1a, modified after Lafay et al., 2017) showing the location of the ophicarbonate outcrops and investigated samples.

Fig. 2. SEM-BSE images of representative textures observed in the Chenaillet ophicarbonates. (a) Serpentine mesh textures with and without C2 calcite partially replacing serpentine in mesh cores (sample RL6). (b) Complex mesh textures showing inner and outer cores surrounded by magnetite; inner cores are locally fully replaced by C2 calcite (sample RL6). (c) Mesh inner and outer cores completely replaced by C2 calcite (sample RL6). (d) Hourglass serpentine associated with magnetite (sample RL9). (e, f) Lizardite+magnetite veinlets (V-1) following original grain boundaries (samples RL3 and RL10). (g) Large lizardite+magnetite vein (V-2) crosscutting mesh textures (sample RL6). (h) C1 calcite vein crosscutting V-2 veins (sample RL6). (i) Textural link between C2 calcite in mesh textures and C1 calcite veins (sample RL10). (j, k) Lizardite+dolomite layers within the C3 calcite matrix containing a relict spinel (Spl); C3 calcite matrix is associated with small chrysotile grains (Ctl) and sometimes crosscut by calcite veins free of serpentine (C3-vein) (sample RL6). (l) Chrysotile grains in C3 calcite matrix (sample RL6). White and red circles are oxygen ($\delta^{18}O_{VSMOW}$, ‰) and carbon ($\delta^{13}C_{VPDB}$, ‰, in parentheses) isotope SIMS pits, respectively. Srp = serpentine, Ctl = chrysotile, Lz = lizardite, Cal = calcite, Dol = dolomite, Mag = magnetite, Spl = Cr-spinel.

Fig. 3. SEM-CL images showing representative CL features in (a-c) C1 calcite veins (samples RL9, RL3 and RL10) and (d-i) C2 calcite mesh (samples RL6, RL10 and RL9). C1 veins are sometimes rimmed by a distinct brighter (b) or darker (c) CL layer.

1134 C2 calcite mesh have marked euhedral (g, i) to anhedral (f, h) CL zonation. Resorption
1135 features are sometimes observed in C2 calcite mesh (f-i). White and red circles are
1136 locations of oxygen ($\delta^{18}O_{VSMOW}$, ‰) and carbon ($\delta^{13}C_{VPDB}$, ‰, in parentheses) isotope
1137 SIMS pits, respectively.
1138 **Fig. 4**. SEM-BSE images of representative dolomite textures in the Chenaillet
1139 ophicarbonates. Dolomite is observed as (a) rims around C2 calcite mesh (sample RL9),
1140 (b) borders along C1 calcite veins at the contact with serpentine (sample RL7), (c)
1141 subhedral grains in the lizardite layers at the boundary between serpentinite clasts and
1142 C3 calcite matrix (sample RL6), (d) borders between C4 calcite vein and serpentinite
1143 clast (sample RL9). White and red circles are oxygen ($\delta^{18}O_{VSMOW}$, ‰) and carbon
1144 ($\delta^{13}C_{VPDB}$, ‰, in parentheses) isotope SIMS pits, respectively.
1145 **Fig. 5**. SEM-CL images showing representative CL features in the carbonate matrix
1146 surrounding serpentinite clasts (samples RL6 and RL10). Domains with large calcite
1147 grains (C1') showing concentric (a-b) or oscillatory CL zoning (c) are surrounded by
1148 an aggregate of fine-grained calcite+chrysotile (a-b). (a, c) Large calcite grains in C1'
1149 domains are crosscut or bounded by calcite veinlets (C1'-veins). (d) Sharp contact
1150 between a calcite C3-vein and the surrounding fine-grained calcite matrix (C3). White
1151 and red circles in (c) and (d) are locations of oxygen ($\delta^{18}O_{VSMOW}$, ‰) and carbon
1152 ($\delta^{13}C_{VPDB}$, ‰, in parentheses) isotope SIMS pits, respectively. Dashed lines in (a) to
1153 (c) are locations of SIMS oxygen and carbon isotope traverses (see Electronic Appendix
1154 B).
1155 **Fig. 6**. Summary of oxygen isotope data in serpentine from the Chenaillet
1156 ophicarbonates measured by SIMS.
1157 **Fig. 7**. Summary of oxygen isotope data in carbonate from the Chenaillet
1158 ophicarbonates measured by SIMS.

1159 **Fig. 8**. Serpentine-magnetite thermometry. (a) Calculation of equilibrium
1160 temperatures for serpentine-magnetite pairs in different textures based on SIMS-
1161 measured mineral $\delta^{18}O$ values. (b) Calculation of water oxygen isotope values in
1162 equilibrium with both serpentine and magnetite in different textures based on
1163 calculated equilibrium temperatures. Solid and dashed lines are calculated equilibrium
1164 temperatures based on serpentine-water oxygen isotope fractionation factors by Früh-
1165 Green et al. (1996) and Saccocia et al. (2009), respectively. Magnetite-water oxygen
1166 isotope fractionation factors are after Bottinga and Javoy (1973).
1167 **Fig. 9**. Serpentine-carbonate thermometry. (a) Calculation of equilibrium
1168 temperatures for lizardite+dolomite and chrysotile+calcite pairs based on SIMS-
1169 measured mineral $\delta^{18}O$ values. (b) Calculation of water oxygen isotope values in
1170 equilibrium with serpentine, dolomite and calcite in each pair based on calculated
1171 equilibrium temperatures. Solid and dashed lines are calculated equilibrium
1172 temperatures for dolomite-serpentine (Matthews and Katz, 1977; Früh-Green et al.,
1173 1996) and calcite-serpentine (O'Neil et al., 1969; Früh-Green et al., 1996),
1174 respectively.
1175 **Fig. 10**. Summary of the different mineral generations and corresponding $\delta^{18}O$ values
1176 (‰). Formation is attributed to four stages of hydrothermal alteration in the Chenaillet
1177 ophicarbonates.
1178 **Fig. 11**. Schematic illustration showing the progression of textural and *T*- $\delta^{18}O_{(water)}$
1179 variations in the Chenaillet ophicarbonates. Ol = olivine, Opx = orthopyroxene, Cr-
1180 Spl = Cr-spinel, Srp_C = serpentine mesh core, Srp_R = serpentine mesh rim, Mag =
1181 magnetite, Lz = lizardite, Dol = dolomite, Ctl = chrysotile. $\delta^{18}O_W$ = oxygen isotope
1182 values of water.

Fig. 12. Simplified cross section showing the evolution of the hydrothermal system presented in this study in a seafloor tectonic setting (modified after Manatschal et al., 2011 and Lafay et al., 2017). Numbers correspond to the stages of alteration shown in Fig. 11.

Table 1. Serpentine-magnetite thermometry for ophicarbonates from the Chenaillet ophiolite.

Table 2. Serpentine-dolomite thermometry in hourglass textures for ophicarbonates from the Chenaillet ophiolite.

SUPPLEMENT FIGURE AND TABLE CAPTIONS

Fig. A.1. SEM-BSE maps of thin sections from the investigated samples from the Chenaillet ophiolite.

Fig. A.2. Diagrams showing the major and minor element chemical composition of serpentine in different textural locations in the various investigated samples. Cal = calcite, Srp = serpentine.

Fig. A.3. SEM-BSE images showing "turbid" calcite domains associated with chrysotile grains (C3) and "clear" calcite domains lacking chrysotile (C1') in the carbonate matrix surrounding serpentinite clasts (Chenaillet ophicarbonates).

Fig. A.4. (a) SIMS oxygen isotope edge-to-edge traverse across a large (~1 mm) C1 calcite vein shown in Fig. 3c. SEM-CL (b) and SEM-BSE (c) images in a different area of the same vein showing ~ 3‰ variation in $\delta^{18}O$ values. White and red circles are locations of oxygen ($\delta^{18}O_{VSMOW}$, ‰) and carbon ($\delta^{13}C_{VPDB}$, ‰, in parentheses) isotope SIMS pits, respectively.

Fig. A.5. Plot of $\delta^{18}O$ versus $\delta^{13}C$ in different calcite generations from the Chenaillet ophicarbonates.

Fig. A.6. BSE-SEM images of SIMS pits on magnetite from the Chenaillet ophicarbonates. (a) Mesh texture (sample RL6), (b) V-1 vein (sample RL3), (c) V-2 vein (sample RL6), and (d) hourglass texture (sample RL9). White areas are remnants of Au coating. White circles are locations of oxygen ($\delta^{18}O_{VSMOW}$, ‰) isotope SIMS pits.

Fig. A.7. Model showing the net variation in oxygen isotope ratios in both serpentine and magnetite as a function of a contemporary variation in temperature and water $\delta^{18}O$. Serpentine-water and magnetite-water oxygen isotope fractionation factors are after Früh-Green et al. (1996) and Bottinga and Javoy (1973), respectively.

Fig. A.8. Representative SEM-BSE images of SIMS pits in serpentine (a), calcite (b), dolomite (c) and magnetite (d).

Table A.1. Complete data table for oxygen isotope analyses by SIMS (A.1a) and corresponding EPMA (A.1b) in serpentine from the Chenaillet ophicarbonates.

Table A.2. Complete data table for oxygen (A.2a) and carbon (A.2b) isotope analyses by SIMS as well as representative EPMA (A.2c) in carbonate from the Chenaillet ophicarbonates.

Table A.3. Complete data table for oxygen isotope analyses in magnetite by SIMS (A.3a) and representative EPMA (A.3b) from the Chenaillet ophicarbonates.

Table A.4. Complete data table for oxygen (A.4a) and carbon (A.4b) isotope analyses by SIMS in carbonate and magnetite (A.4c) reference materials. Data on serpentine reference materials are published in Scicchitano et al. (2020) in supplementary Table S2 (sessions S6 and S8).

1233 **Table A.5**. Serpentine-magnetite thermometry for ophicarbonates from the Chenaillet

1234 ophiolite using different serpentine-magnetite calibrations.

1235 **Table 1**. Serpentine-magnetite thermometry for ophicarbonates from the Chenaillet ophiolite.

Analysis ID	Texture	$\delta^{18}O$ (‰) *serpentine*	$\delta^{18}O$ (‰) *magnetite*	$\Delta^{18}O$(Srp-Mag)	*T* (°C)* *calculated*	$\delta^{18}O_w$ (‰)* *calculated*	*T* (°C)** *calculated*	$\delta^{18}O_w$ (‰)** *calculated*
RL6-1-(Srp-18b/Mag-1)	mesh	6.6	-6.0	12.7	196	4.3	245	3.1
RL6-1-(Srp-18b/Mag-2)	mesh	6.6	-5.6	12.2	204	4.5	252	3.4
RL6-1-(Srp-20/Mag-3)	mesh	6.7	-5.7	12.5	199	4.5	248	3.4
RL6-1-(Srp-34/Mag-4)	mesh	6.6	-10.2	16.9	136	2.1	194	0.0
RL6-1-(Srp-24/Mag-5)	mesh	7.8	-6.3	14.2	172	4.7	225	3.2
RL6-1-(Srp-25/Mag-7)	mesh	7.4	-5.5	12.9	192	5.0	242	3.7
RL6-1-(Srp-27/Mag-8)	mesh	6.3	-9.8	16.3	144	2.2	201	0.3
RL6-1-(Srp-29/Mag-9)	mesh	6.8	-6.3	13.2	188	4.2	239	2.9
RL6-1-(Srp-41/Mag-17)	mesh	7.2	-5.1	12.3	202	5.1	250	3.9
RL6-1-(Srp-42/Mag-18)	mesh	7.4	-5.6	13.1	188	4.9	239	3.6
RL6-1-(Srp-50/Mag-19)	mesh	5.2	-9.6	15.0	161	1.8	216	0.1
RL6-1-(Srp-49/Mag-21)	mesh	6.9	-10.2	17.3	132	2.2	191	0.1
RL6-1-(Srp-49/Mag-22)	mesh	6.9	-9.5	16.5	141	2.6	198	0.6
RL6-2-(Srp-28/Mag-13)	mesh	7.4	-5.0	12.6	198	5.2	247	4.0
RL6-2-(Srp-27/Mag-14)	mesh	7.2	-7.6	14.9	162	3.7	217	2.1
RL6-2-(Srp-26/Mag-15)	mesh	7.5	-7.9	15.5	154	3.7	210	2.0
RL6-2-(Srp25/Mag-16)	mesh	7.4	-8.0	15.6	153	3.7	209	1.9
RL6-2-(Srp-13/Mag-5)	V-2 vein	4.1	-10.1	14.4	169	1.0	223	-0.6
RL6-2-(Srp-18/Mag-10)	V-2 vein	3.8	-7.7	11.6	215	2.0	261	1.1
RL3-(Srp-43/Mag-5)	V-1 vein	5.8	-8.2	14.1	173	2.8	226	1.3
RL9-(Srp-54/Mag-16)	hourglass Srp	5.2	-9.6	14.9	162	1.8	216	0.1
RL9-(Srp-58/Mag-18)	hourglass Srp	4.5	-8.4	13.1	190	2.0	240	0.7
RL9-(Srp-57/Mag-19)	hourglass Srp	4.6	-9.1	13.8	178	1.7	230	0.3
RL9-(Srp-56/Mag-20)	hourglass Srp	4.5	-8.0	12.5	198	2.3	247	1.1

* Srp-water after Früh-Green et al. (1996), ** Srp-water after Saccocia et al. (2009). Mag-water are after Bottinga and Javoy (1973). $\delta^{18}O_w$ = calculated oxygen isotope value of water in equilibrium with serpentine and magnetite.

1236
1237

1238 **Table 2**. Serpentine-dolomite thermometry in hourglass textures for ophicarbonates from the Chenaillet ophiolite.

Analysis ID	Texture	$\delta^{18}O$ (‰) *serpentine*	$\delta^{18}O$ (‰) *dolomite*	$\Delta^{18}O$(Dol-Srp)	*T* (°C) *calculated*	$\delta^{18}O_w$ (‰) *calculated*
RL9-1-(Srp-1/Dol-1)	hourglass	4.3	11.8	7.5	228	2.9
RL9-1-(Srp-4/Dol-2)	hourglass	4.4	11.7	7.3	235	3.1
RL9-1-(Srp-6/Dol-4)	hourglass	4.1	12.6	8.5	190	1.6
RL9-1-(Srp-10/Dol-5)	hourglass	4.3	12.0	7.6	220	2.7
RL9-1-(Srp-26/Dol-6)	hourglass	4.8	12.6	7.8	215	3.0
RL9-1-(Srp-29/Dol-10)	hourglass	4.3	12.2	7.9	213	2.5
RL9-1-(Srp-46/Dol-14)	hourglass	4.3	10.1	5.8	315	4.5
RL9-1-(Srp-51/Dol-15)	hourglass	4.3	12.5	8.2	200	2.1
RL9-1-(Srp-59/Dol-19)	hourglass	4.2	11.2	7.0	250	3.2
RL7-(Srp-4/Dol-4)	hourglass	4.6	10.9	6.3	285	4.3
RL7-(Srp-10/Dol-2)	hourglass	5.6	11.8	6.2	290	5.4
RL7-(Srp-9/Dol-1)	hourglass	5.0	11.6	6.6	270	4.4

1239 Srp-water after Früh-Green et al. (1996), Dol-water after Matthews and Katz (1977). $\delta^{18}O_w$ = calculated oxygen isotope value of water in equilibrium with serpentine and
1240 dolomite.
1241

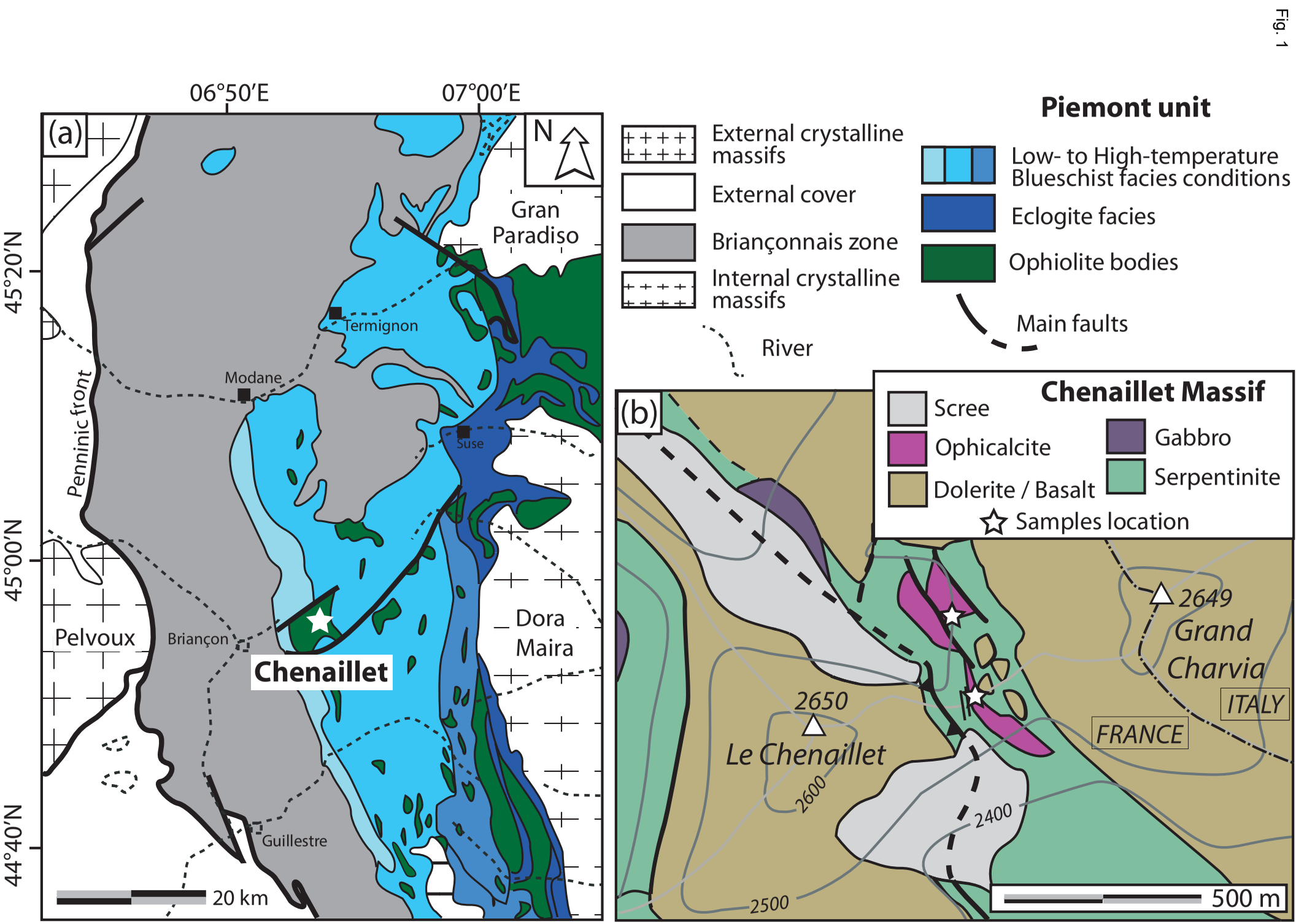
Fig. 1
(a)
06°50'E
07°00'E
45°20'N
45°00'N
44°40'N
N
Gran Paradiso
Termignon
Modane
Suse
Penninic front
Pelvoux
Briançon
Chenaillet
Dora Maira
Guillestre
20 km
External crystalline massifs
External cover
Briançonnais zone
Internal crystalline massifs
River
Piemont unit
Low- to High-temperature Blueschist facies conditions
Eclogite facies
Ophiolite bodies
Main faults
(b)
Chenaillet Massif
Scree
Ophicalcite
Dolerite / Basalt
Gabbro
Serpentinite
Samples location
2649
Grand Charvia
ITALY
FRANCE
2650
Le Chenaillet
2600
2400
2500
500 m

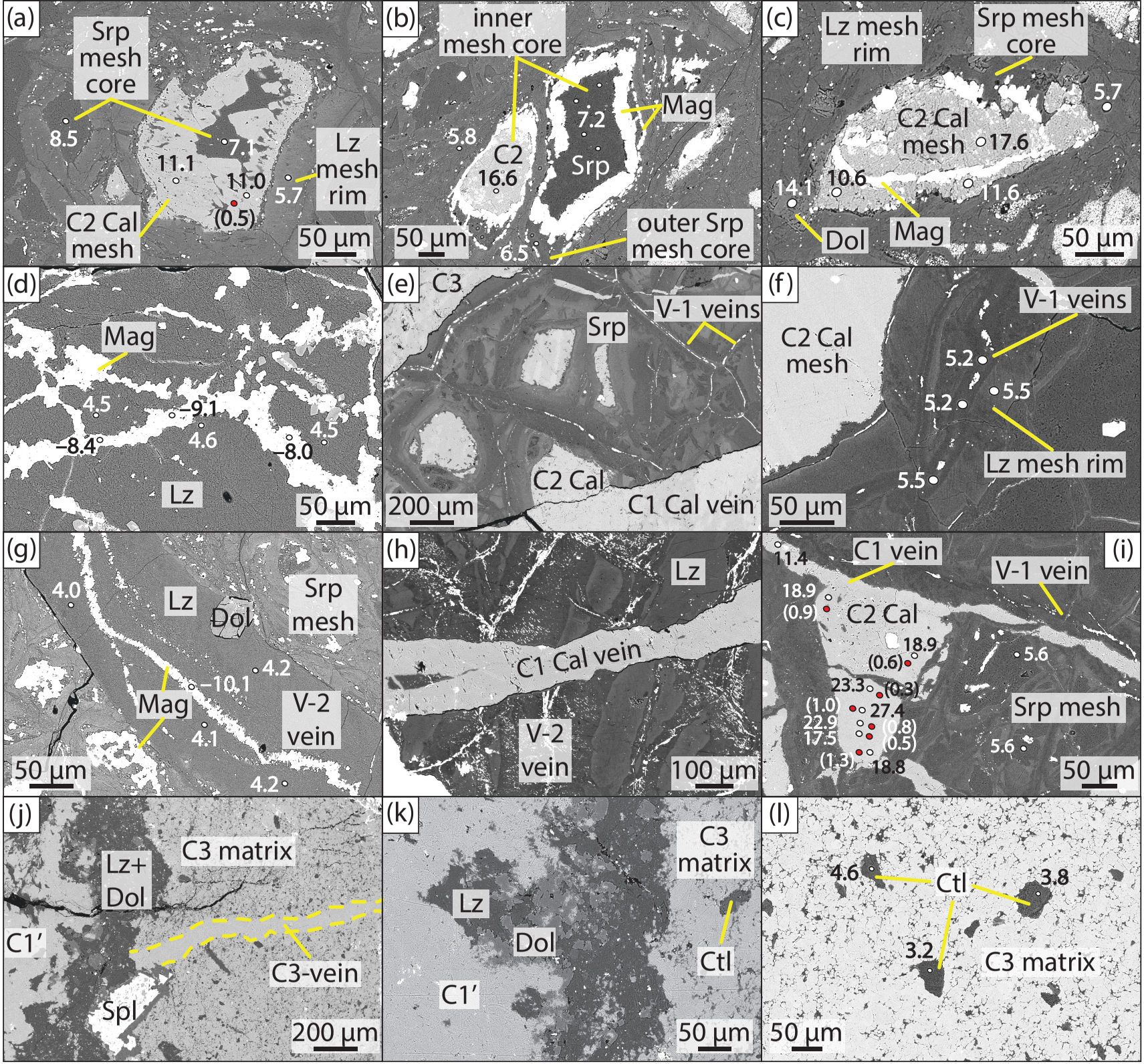
(a)
Srp mesh core
8.5
7.1
11.1
11.0
5.7
Lz mesh rim
(0.5)
C2 Cal mesh
50 µm
(b)
inner mesh core
Mag
7.2
5.8
C2
16.6
Srp
50 µm
6.5
outer Srp mesh core
(c)
Lz mesh rim
Srp mesh core
5.7
C2 Cal mesh
17.6
14.1
10.6
11.6
Dol
Mag
50 µm
(d)
Mag
4.5
−9.1
4.6
4.5
−8.4
−8.0
Lz
50 µm
(e)
C3
Srp
V-1 veins
C2 Cal
C1 Cal vein
200 µm
(f)
V-1 veins
C2 Cal mesh
5.2
5.5
5.2
Lz mesh rim
5.5
50 µm
(g)
4.0
Lz
Dol
Srp mesh
4.2
−10.1
Mag
V-2 vein
4.1
50 µm
4.2
(h)
Lz
C1 Cal vein
V-2 vein
100 µm
(i)
11.4
C1 vein
V-1 vein
18.9
(0.9)
C2 Cal
18.9
(0.6)
5.6
23.3
(0.3)
(1.0)
27.4
Srp mesh
22.9
(0.8)
17.5
(0.5)
5.6
(1.3)
18.8
50 µm
(j)
Lz+ Dol
C3 matrix
C1′
C3-vein
Spl
200 µm
(k)
C3 matrix
Lz
Dol
Ctl
C1′
50 µm
(l)
4.6
Ctl
3.8
3.2
C3 matrix
50 µm

Fig. 2

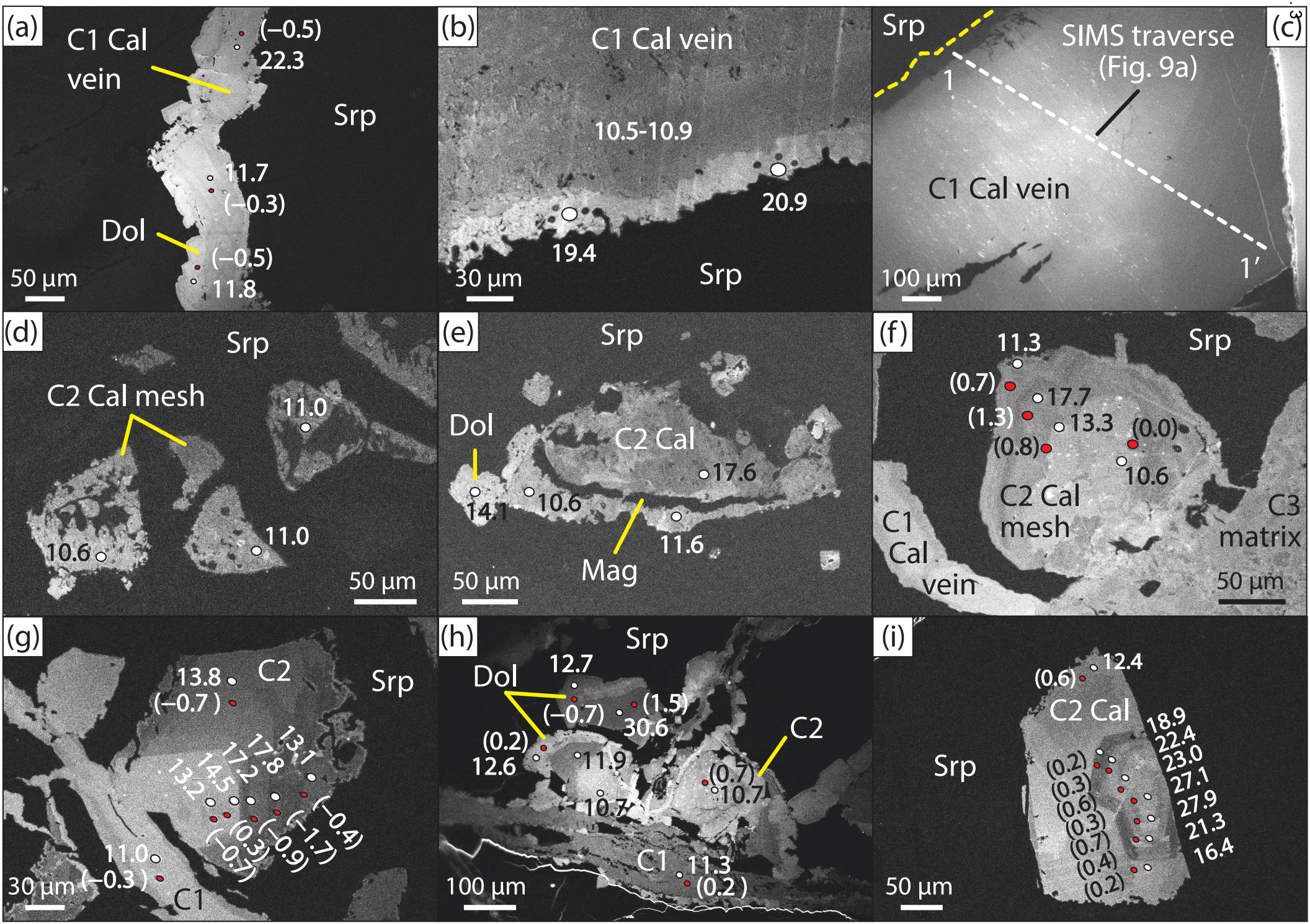
(a)
C1 Cal vein
(–0.5)
22.3
Srp
11.7
(–0.3)
Dol
(–0.5)
11.8
50 µm
(b)
C1 Cal vein
10.5-10.9
20.9
19.4
30 µm
Srp
(c)
Srp
SIMS traverse (Fig. 9a)
1
C1 Cal vein
1′
100 µm
(d)
Srp
C2 Cal mesh
11.0
11.0
10.6
50 µm
(e)
Srp
Dol
C2 Cal
17.6
14.1
10.6
11.6
Mag
50 µm
(f)
11.3
Srp
(0.7)
17.7
(1.3)
13.3
(0.0)
(0.8)
10.6
C2 Cal mesh
C3 matrix
C1 Cal vein
50 µm
(g)
13.8
C2
Srp
(–0.7)
13.1
17.8
17.2
14.5
13.2
(–0.4)
(–1.7)
(–0.9)
(0.3)
(–0.7)
11.0
(–0.3)
30 µm
C1
(h)
Srp
12.7
Dol
(–0.7)
(1.5)
30.6
(0.2)
12.6
11.9
C2
(0.7)
10.7
10.7
C1
11.3
(0.2)
100 µm
(i)
12.4
(0.6)
C2 Cal
18.9
22.4
23.0
27.1
27.9
21.3
16.4
Srp
(0.2)
(0.3)
(0.6)
(0.3)
(0.7)
(0.4)
(0.2)
50 µm

Fig. 3

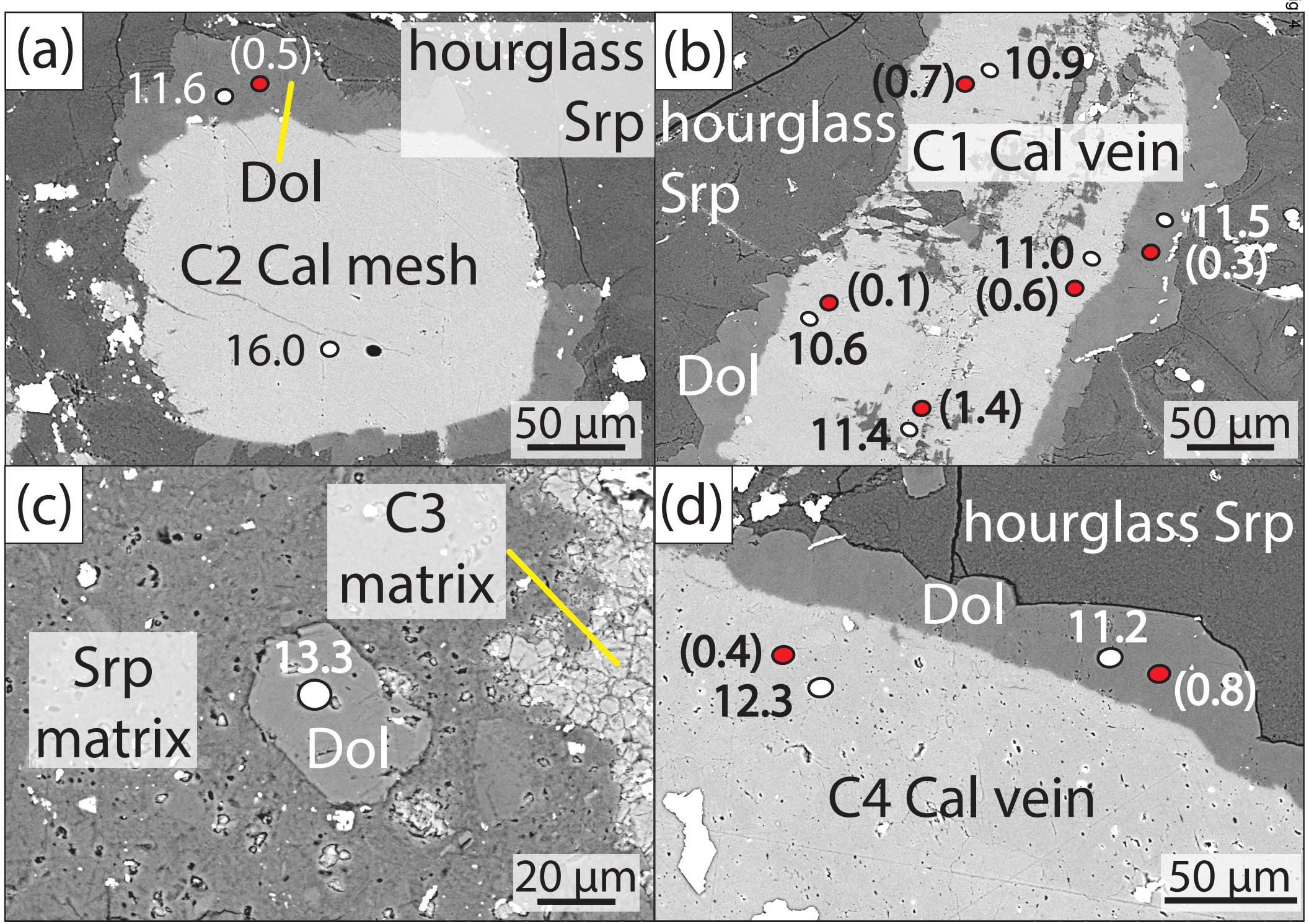
(a)
(0.5)
11.6
hourglass Srp
Dol
C2 Cal mesh
16.0
50 µm
(b)
(0.7)
10.9
hourglass Srp
C1 Cal vein
11.5
(0.3)
11.0
(0.1)
(0.6)
10.6
Dol
(1.4)
11.4
50 µm
(c)
C3 matrix
Srp matrix
13.3
Dol
20 µm
(d)
hourglass Srp
Dol
11.2
(0.4)
(0.8)
12.3
C4 Cal vein
50 µm

Fig 4

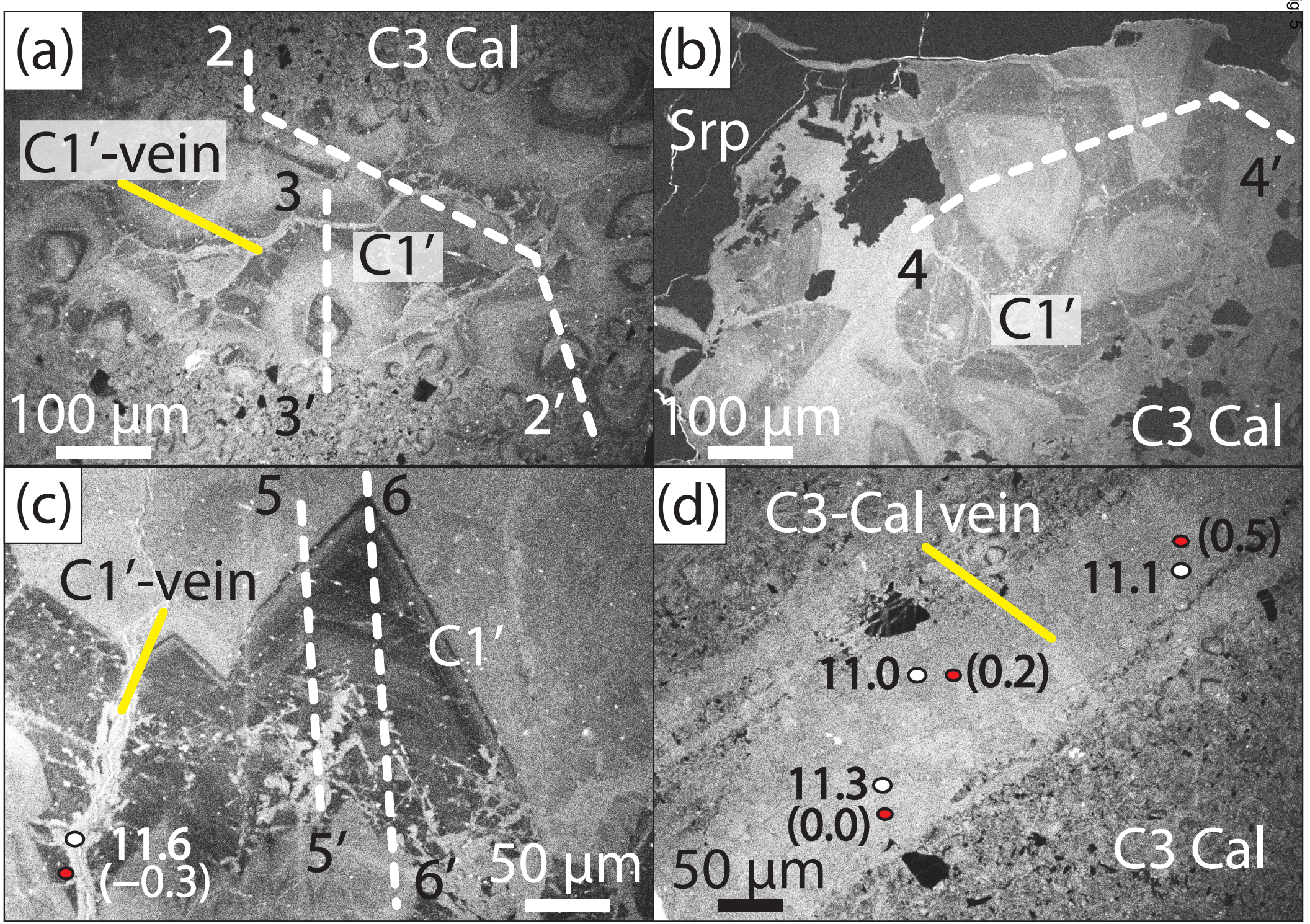
(a)
2
C3 Cal
C1′-vein
3
C1′
100 μm
3′
2′
(b)
Srp
4′
4
C1′
100 μm
C3 Cal
(c)
5
6
C1′-vein
C1′
11.6
(–0.3)
5′
6′
50 μm
(d)
C3-Cal vein
(0.5)
11.1
11.0
(0.2)
11.3
(0.0)
50 μm
C3 Cal

Fig. 5

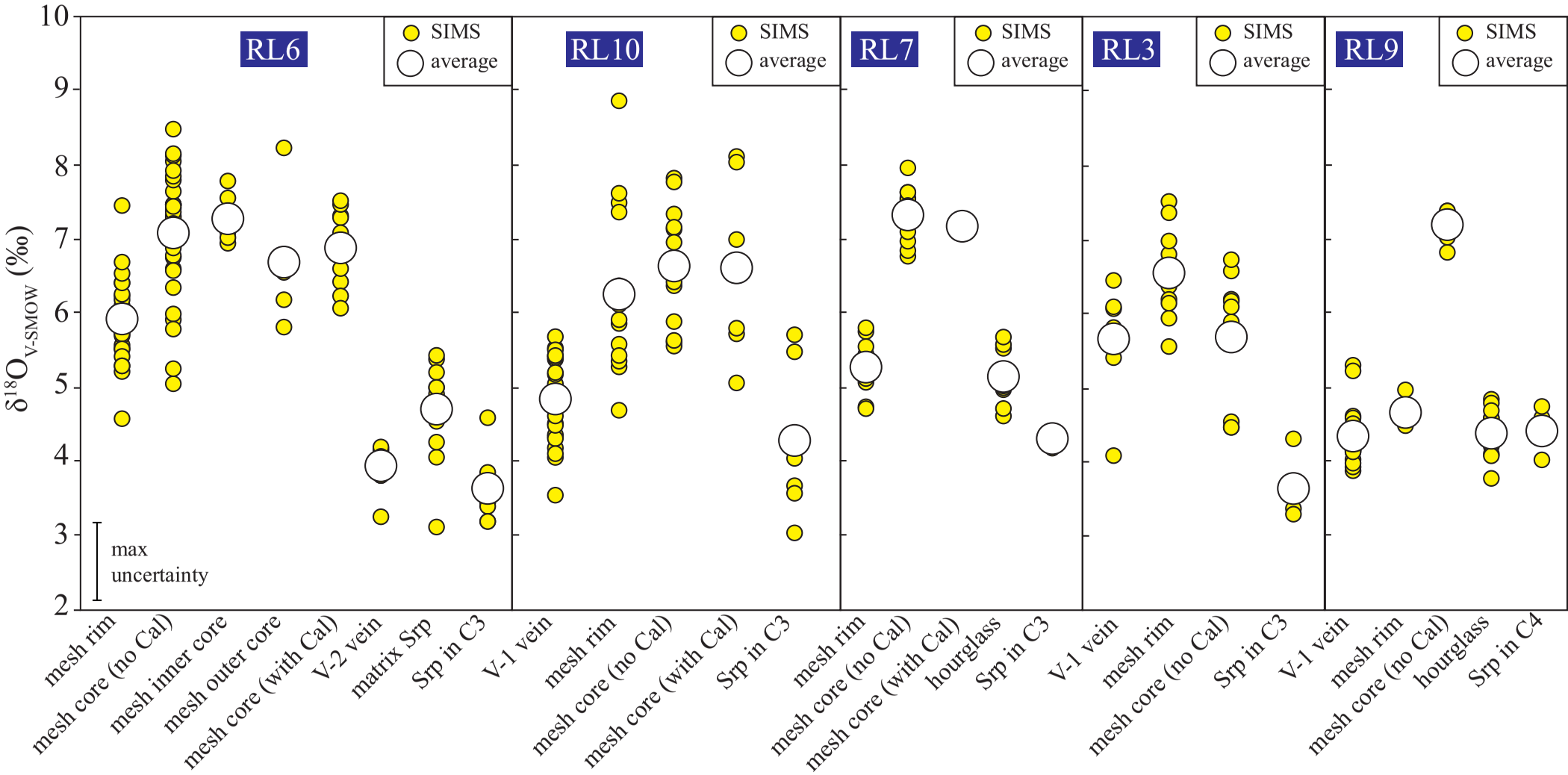
RL6
RL10
RL7
RL3
RL9
SIMS
average
max
uncertainty
$\delta^{18}O_{V\text{-}SMOW}$ (‰)
10
9
8
7
6
5
4
3
2
mesh rim
mesh core (no Cal)
mesh inner core
mesh outer core
mesh core (with Cal)
V-2 vein
matrix Srp
Srp in C3
V-1 vein
mesh rim
mesh core (no Cal)
mesh core (with Cal)
Srp in C3
mesh rim
mesh core (no Cal)
mesh core (with Cal)
hourglass
Srp in C3
V-1 vein
mesh rim
mesh core (no Cal)
Srp in C3
V-1 vein
mesh rim
mesh core (no Cal)
hourglass
Srp in C4

Fig. 6

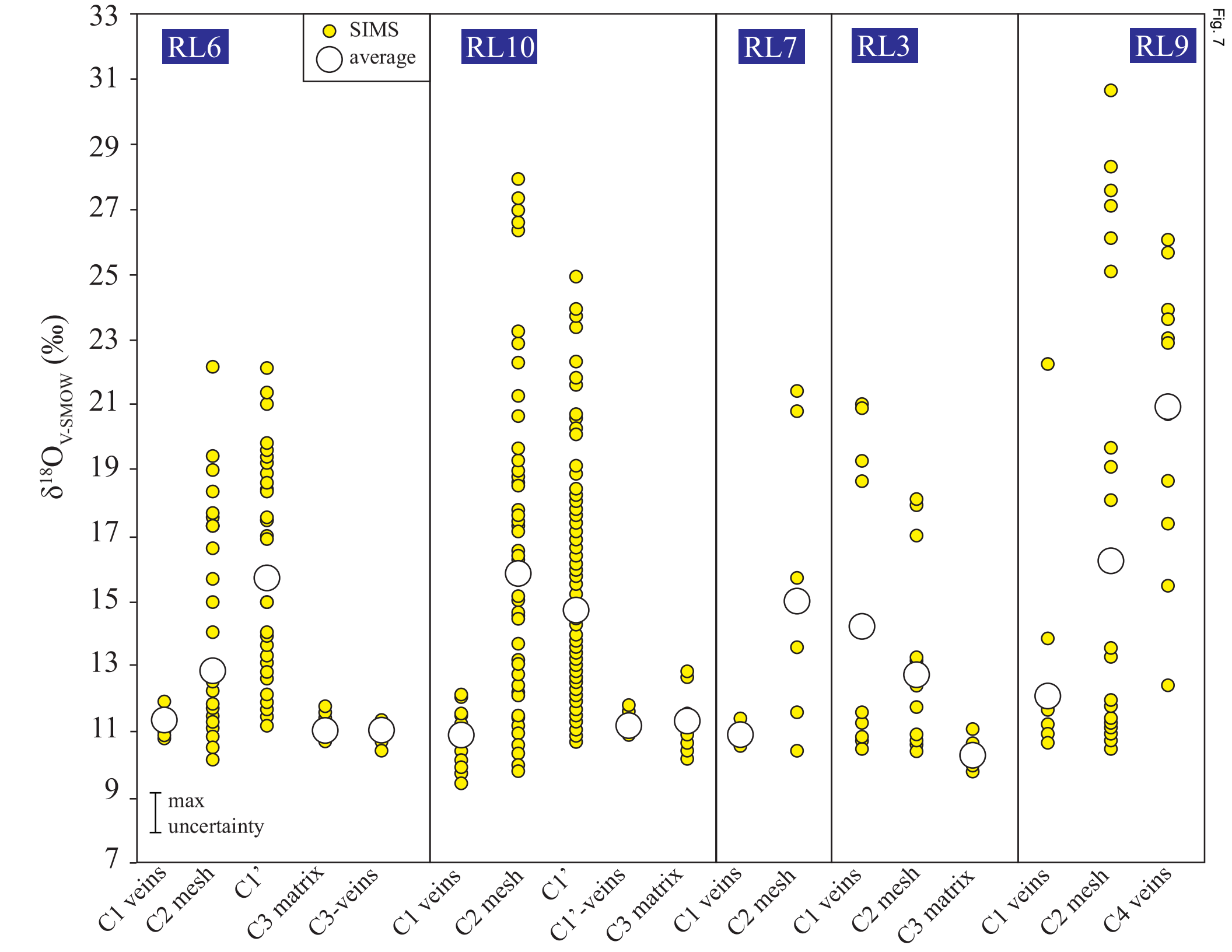
RL6
RL10
RL7
RL3
RL9
SIMS
average
max
uncertainty
$\delta^{18}O_{V\text{-}SMOW}$ (‰)
33
31
29
27
25
23
21
19
17
15
13
11
9
7
C1 veins
C2 mesh
C1'
C3 matrix
C3-veins
C1 veins
C2 mesh
C1'
C1'-veins
C3 matrix
C1 veins
C2 mesh
C1 veins
C2 mesh
C3 matrix
C1 veins
C2 mesh
C4 veins

Fig. 7

Fig. 8

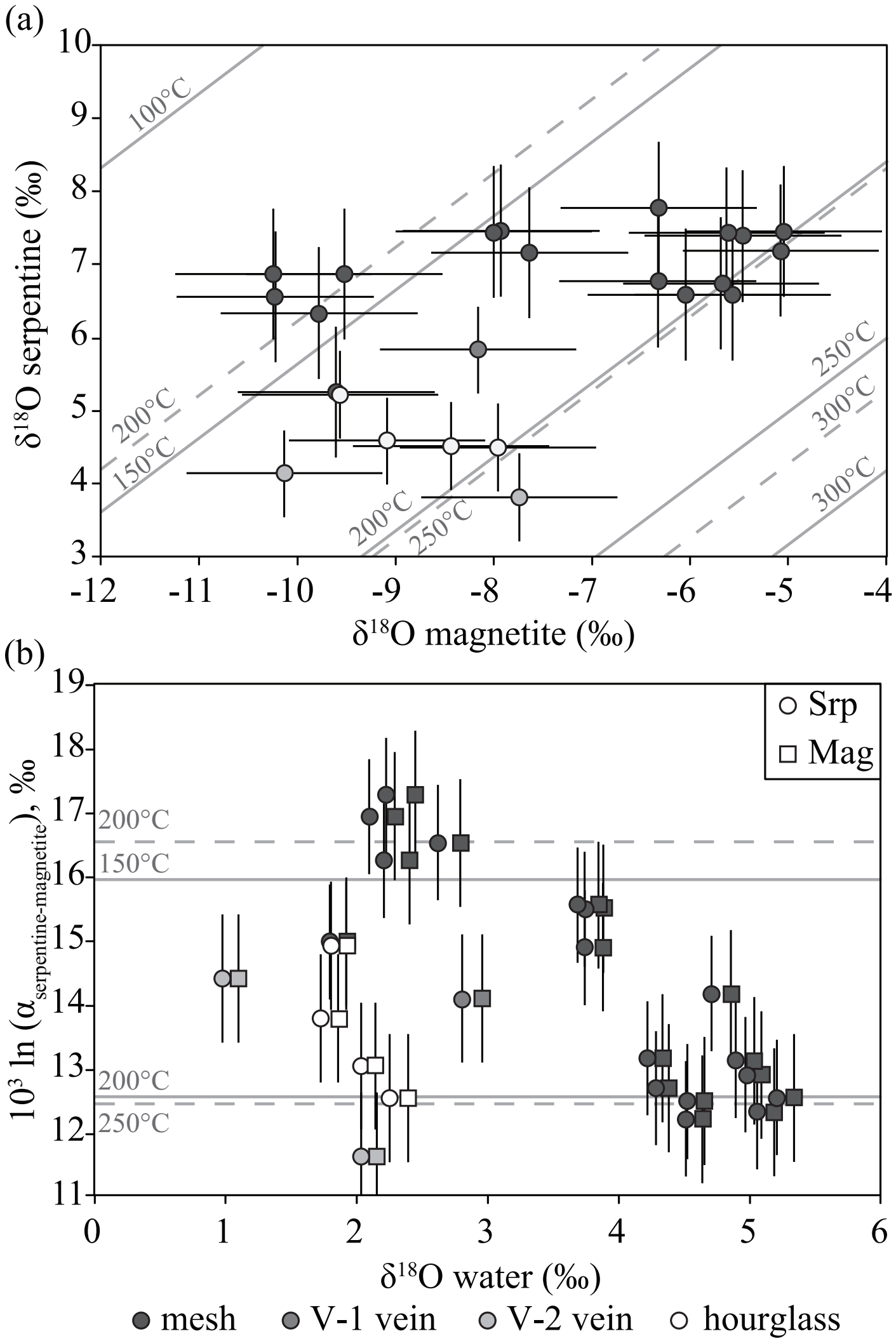
(a)
100°C
200°C
150°C
250°C
300°C
200°C
250°C
300°C
δ18O serpentine (‰)
δ18O magnetite (‰)
(b)
Srp
Mag
200°C
150°C
200°C
250°C
10³ ln (αserpentine-magnetite), ‰
δ18O water (‰)
mesh
V-1 vein
V-2 vein
hourglass

Fig. 9

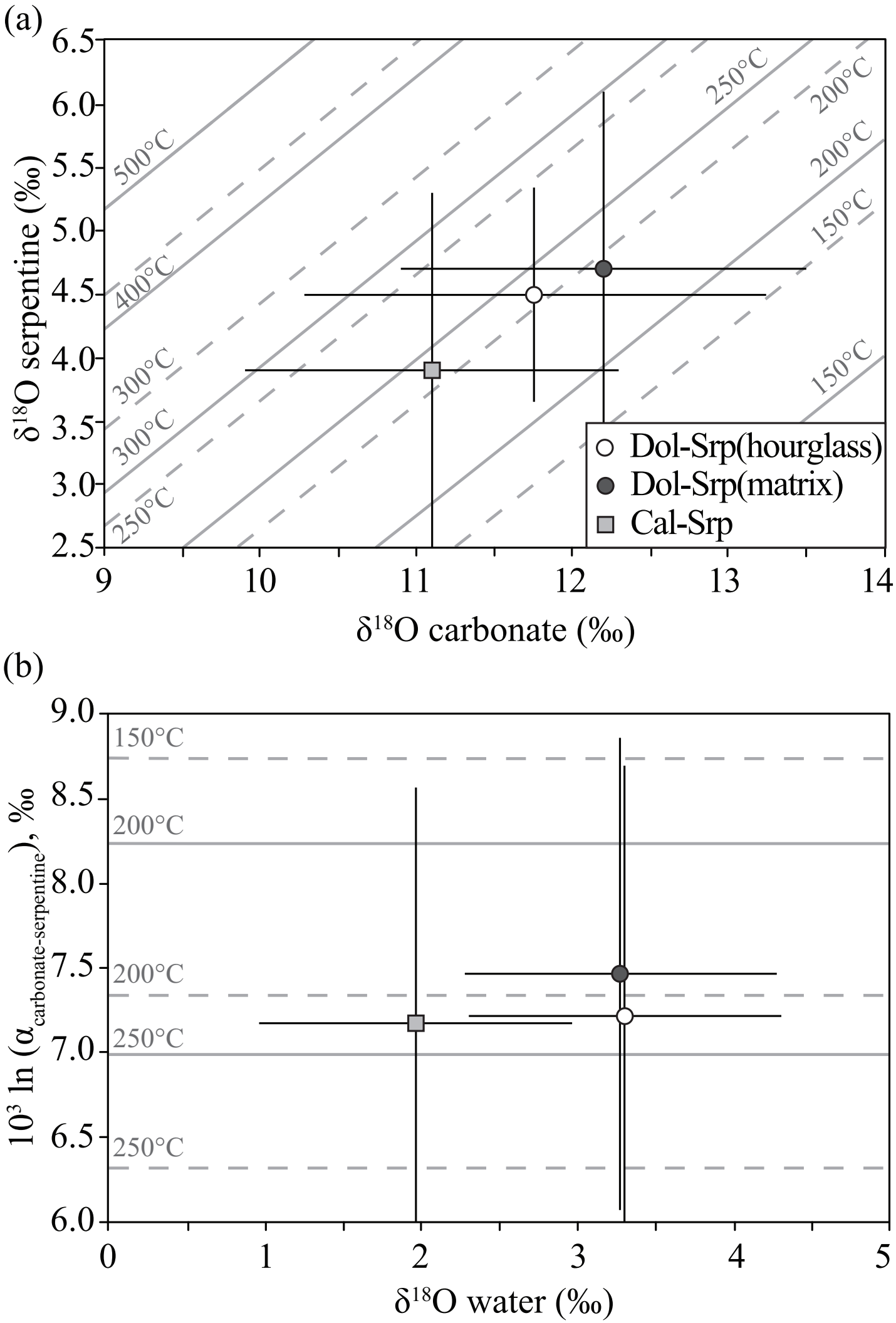
(a)
6.5
6.0
5.5
5.0
4.5
4.0
3.5
3.0
2.5
δ18O serpentine (‰)
500°C
400°C
300°C
300°C
250°C
250°C
200°C
200°C
150°C
150°C
Dol-Srp(hourglass)
Dol-Srp(matrix)
Cal-Srp
9
10
11
12
13
14
δ18O carbonate (‰)
(b)
9.0
8.5
8.0
7.5
7.0
6.5
6.0
10³ ln (αcarbonate-serpentine), ‰
150°C
200°C
200°C
250°C
250°C
0
1
2
3
4
5
δ18O water (‰)

Fig. 10

Stages / Minerals	Early Serpentinization: T_{min} = 130-200 °C	Low-T Carbonation: T_{min} = 10 °C	High-T Serpentinization & Carbonation: T = 160-240 °C	Late Carbonate Veining: T_{min} = 40-70 °C
Serpentine V-1 veins	3.5 to 6.4‰			
Serpentine mesh rims	4.5 to 8.8‰			
Serpentine mesh cores	4.4 to 8.5‰			
Magnetite V-1 veins	-8.5 to -7.3‰			
Magnetite mesh	-10.6 to -5.0‰			
Calcite C1 veins		22.3 to 9.4‰		
Calcite C2 mesh		30.6 to 9.8‰		
Calcite C1’		24.9 to 10.6‰		
Serpentine V-2 veins			3.2 to 4.2‰	
Serpentine hourglass			3.8 to 5.7‰	
Magnetite V-2 veins			-10.6 to -7.7‰	
Magnetite hourglass			-9.6 to -8.0‰	
Serpentine matrix			3.1 to 5.4‰	
Serpentine in C3 matrix			3.0 to 5.7‰	
Calcite C3 matrix			9.8 to 12.9‰	
Calcite C3-veins			10.5 to 11.5‰	
Calcite C1’-veins			10.9 to 11.8‰	
Dolomite		10.1 to 14.1‰	11.4 to 13.2‰	11.2 to 12.5‰
Calcite C4 vein				12.3 to 26.0‰
Serpentine in C4 vein				4.0 to 4.8‰

Fig. 11

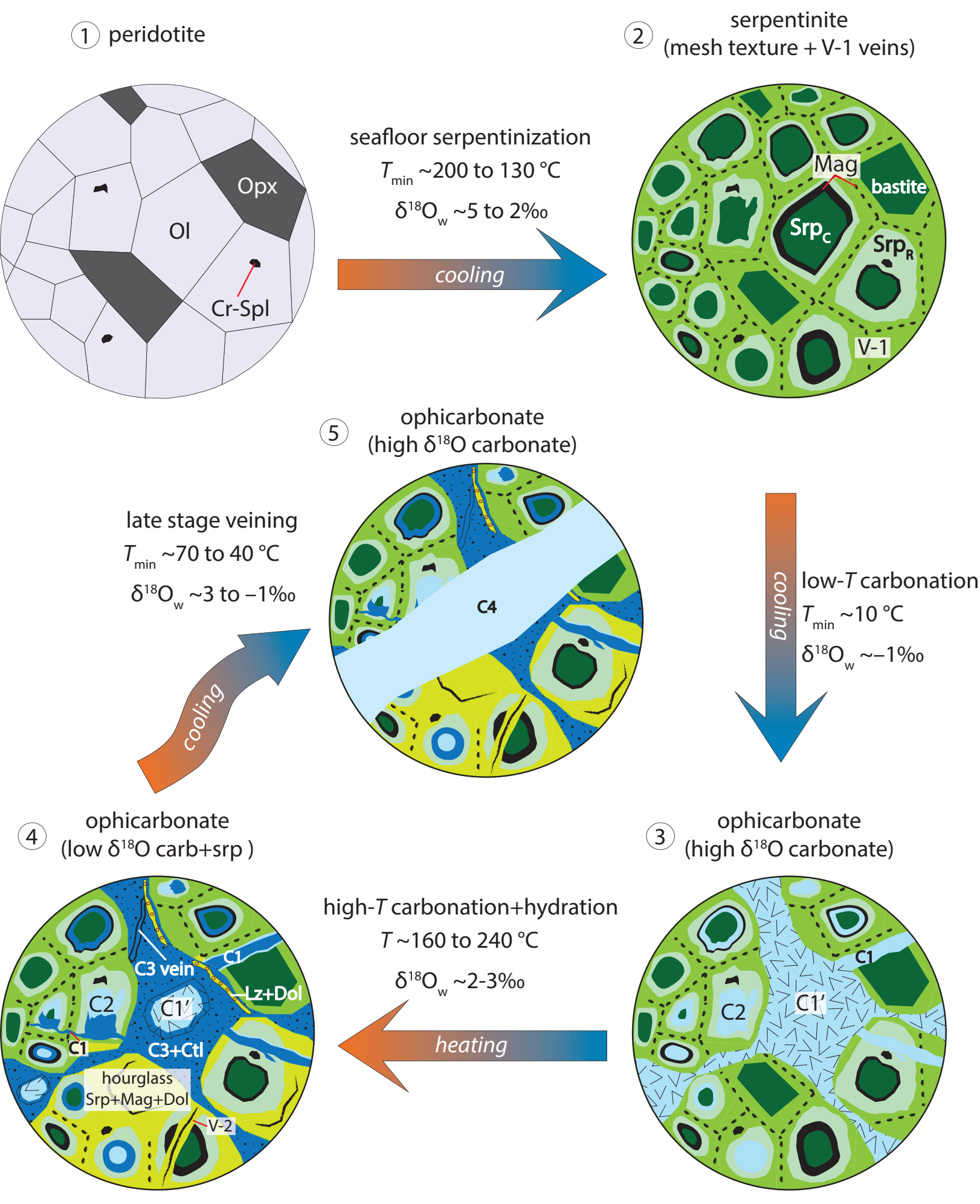
1 peridotite
Opx
Ol
Cr-Spl
seafloor serpentinization
T_{min} ~200 to 130 °C
$\delta^{18}O_w$ ~5 to 2‰
cooling
2 serpentinite
(mesh texture + V-1 veins)
Mag
bastite
Srp_C
Srp_R
V-1
5 ophicarbonate
(high $\delta^{18}O$ carbonate)
C4
late stage veining
T_{min} ~70 to 40 °C
$\delta^{18}O_w$ ~3 to –1‰
cooling
cooling
low-T carbonation
T_{min} ~10 °C
$\delta^{18}O_w$ ~–1‰
4 ophicarbonate
(low $\delta^{18}O$ carb+srp)
C3 vein
C1
Lz+Dol
C2
C1′
C1
C3+Ctl
hourglass
Srp+Mag+Dol
V-2
high-T carbonation+hydration
T ~160 to 240 °C
$\delta^{18}O_w$ ~2-3‰
heating
3 ophicarbonate
(high $\delta^{18}O$ carbonate)
C1
C2
C1′

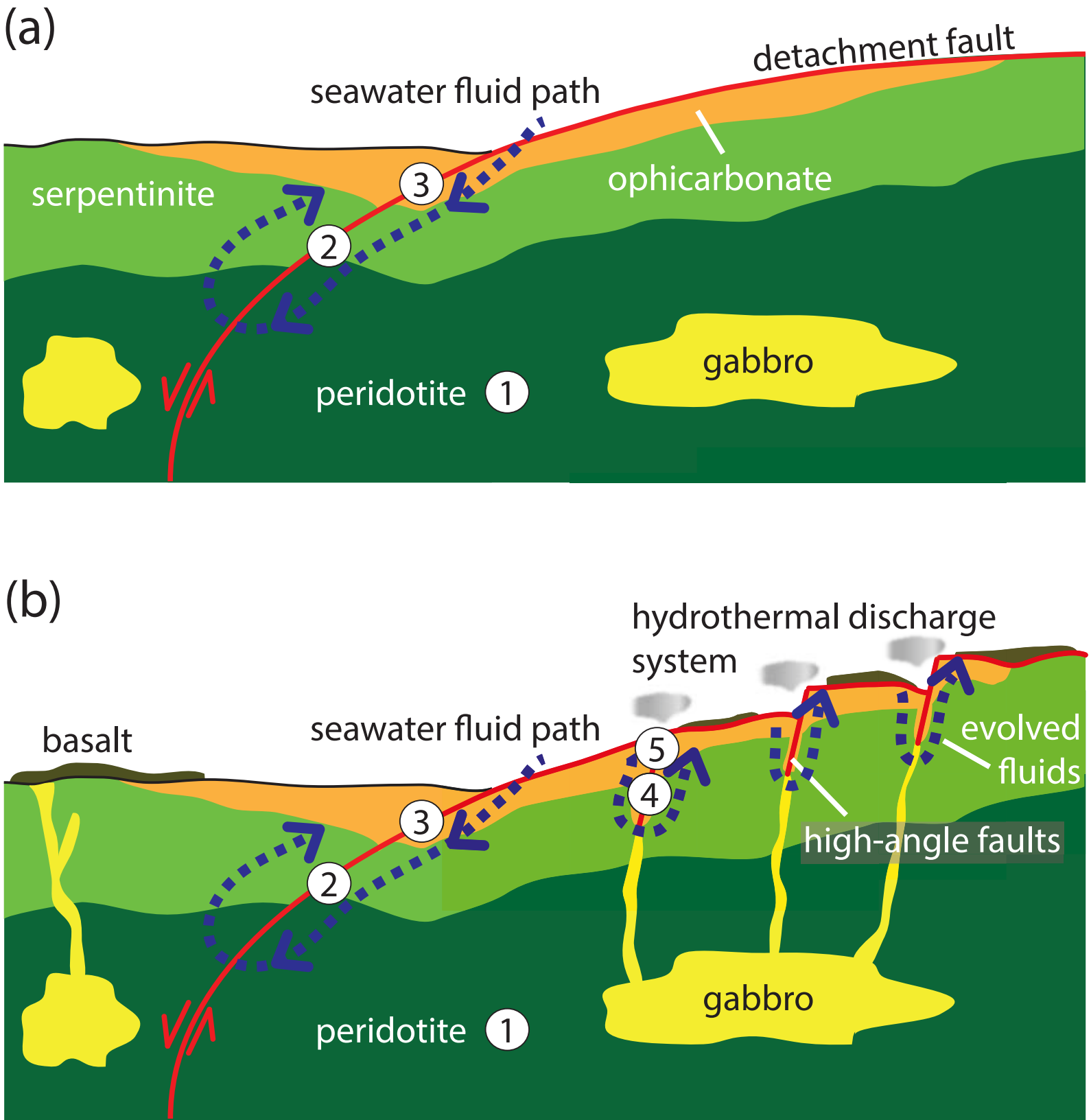
(a)
detachment fault
seawater fluid path
serpentinite
ophicarbonate
3
2
gabbro
peridotite
1
(b)
hydrothermal discharge system
basalt
seawater fluid path
5
4
evolved fluids
3
high-angle faults
2
gabbro
peridotite
1

Fig. 12